

See discussions, stats, and author profiles for this publication at: <https://www.researchgate.net/publication/285245148>

Optical processors as conceptual tools for designing nonconventional devices

ARTICLE · JANUARY 2015

DOI: 10.1007/978-94-017-9481-7_8

READS

12

5 AUTHORS, INCLUDING:



[Jorge Ojeda-Castaneda](#)

Universidad de Guanajuato

254 PUBLICATIONS 1,984 CITATIONS

[SEE PROFILE](#)



[Sergio Ledesma](#)

Universidad de Guanajuato

76 PUBLICATIONS 144 CITATIONS

[SEE PROFILE](#)



[Cristina M Gómez-Sarabia](#)

Universidad de Guanajuato

37 PUBLICATIONS 112 CITATIONS

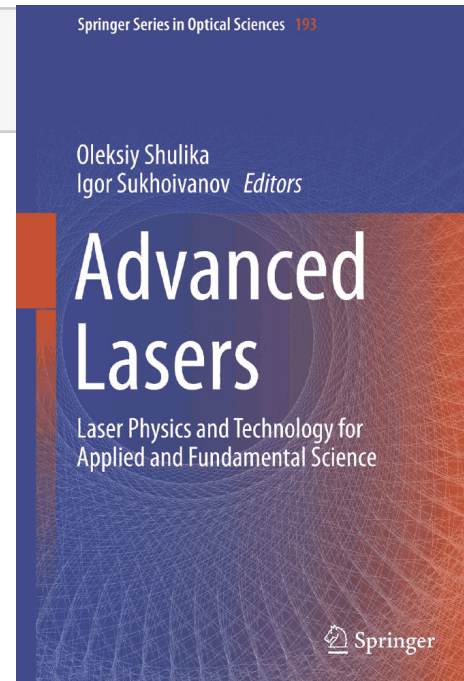
[SEE PROFILE](#)

ISSN 0342-4111 ISSN 1556-1534 (electronic)

[Springer Series in Optical Sciences](#)

ISBN 978-94-017-9480-0 ISBN 978-94-017-9481-7 (eBook)

DOI 10.1007/978-94-017-9481-7



Chapter 8

Advanced Lasers

Volume 193 of the series Springer Series in Optical Sciences pp 117-146

Date: 29 April 2015

Optical Processors as Conceptual Tools for Designing Nonconventional Devices

Jorge Ojeda-Castañeda, Sergio Ledesma, Emmanuel Yépez-Vidal, Cristina M. Gomez-Sarabia, Miguel Torres-Cisneros

Abstract

We discuss the use of nonconventional optical processors for generating irradiance distributions, which are useful for visualizing the characteristics of imaging devices that extend the depth of field. Our discussion starts with the use of binary masks for generating nonconventional irradiance distributions, which display the variations of the impulse response with focus errors. By using an anamorphic optical processor these irradiance distributions can easily be transformed into variations of the optical transfer function vs focus errors. Next, another anamorphic optical processor is used for generating the ambiguity function of a pupil aperture, which helps to visualize the variations of the optical transfer function with variable focus error. Finally, we translate the integral transform associated with the evaluation of the ambiguity function into tunable devices for controlling the depth of field, without modifying the size of the pupil aperture.

Keywords

Imaging devices Optical processors Optical visualization Extended depth of field Pupil engineering Apodization Phase-only masks Ambiguity function Wigner distribution Phase-space optics

Front Matter Pages i-ix

Chapter 1 Pages 1-17

Recent Progress in Polarization-Bistable VCSELs and Their Applications to All-Optical Signal Processing

Chapter 2 Pages 19-33

Tunable Lasers Based on Multimode Interference Effects

Daniel A. May-Arrioja, José E. Antonio-Lopez, José J. Sanchez-Mondragón, P. LiKamWa

Chapter 3 Pages 35-48

Whispering Gallery Mode Microdisk Resonator with Dynamic Material Properties

Nataliya Sakhnenko

Chapter 4 Pages 49-69

Superradiant Lasing and Collective Dynamics of Active Centers with Polarization Lifetime Exceeding Photon Lifetime

Vi. V. Kocharovsky, A. A. Belyanin, E. R. Kocharovskaya, V. V. Kocharovsky

Chapter 5 Pages 71-84

The Control of Energy, Temporal and Spatial Characteristics a Microchip Laser with Active Output Mirror

V. V. Kiyko, V. A. Kondratyev, S. V. Gagarsky, E. N. Ofitserov, A. G. Suzdaltsev

Chapter 6 Pages 85-100

Recent Advances in Secure Transmission with Chaotic Carriers

Silvano Donati, Valerio Annovazzi-Lodi

Chapter 7 Pages 101-115

Superwicking Surfaces Produced by Femtosecond Laser

A. Y. Vorobyev, Chunlei Guo

Chapter 8 Pages 117-146

Optical Processors as Conceptual Tools for Designing Nonconventional Devices

Jorge Ojeda-Castañeda, Sergio Ledesma, Emmanuel Yépez-Vidal, Cristina M. Gomez-Sarabia, Miguel Torres-Cisneros.

Chapter 9 Pages 147-158

Description of the Dynamics of Charged Particles in Electric Fields: An Approach Using Fractional Calculus

F. Gómez-Aguilar, E. Alvarado-Méndez

Chapter 10 Pages 159-172

Sub- and Nanosecond Pulsed Lasers Applied to the Generation of Broad Spectrum in Standard and Microstructured Optical Fibers

Julián M. Estudillo-Ayala, Roberto Rojas-Laguna, Juan C. Hernández García

Chapter 11 Pages 173-181

Extremely High Power CO₂ Laser Beam Correction

Alexis Kudryashov, Alexander Alexandrov, Alexey Rukosuev, Vadim Samarkin

Chapter 12 Pages 183-197

Measurements of Intense and Wide-Aperture Laser Radiation Parameters with Thinwire Bolometers

S. V. Pogorelov

Chapter 13 Pages 199-212

Spectral and Lasing Characteristics of Some Red and Nir Laser Dyes in Silica Matrices

I. M. Pritula, O. N. Bezkravnaya, V. M. Puzikov, V.V. Maslov, A. G. Plaksey.

Chapter 14 Pages 213-230

Interpretation of the Time Delay in the Ionization of Coulomb Systems by Attosecond Laser Pulses

Vladislav V. Serov, Vladimir L. Derbov, Tatyana A. Sergeeva

Oleksiy Shulika
Igor Sukhoivanov *Editors*

Advanced Lasers

Laser Physics and Technology for
Applied and Fundamental Science



Springer

Springer Series in Optical Sciences

Volume 193

Editor-in-chief

William T. Rhodes, Florida, USA

Series Editors

Ali Adibi, Atlanta, USA

Theodor W. Hänsch, Garching, Germany

Ferenc Krausz, Garching, Germany

Barry R. Masters, Cambridge, USA

Katsumi Midorikawa, Saitama, Japan

Herbert Venghaus, Berlin, Germany

Horst Weber, Berlin, Germany

Harald Weinfurter, München, Germany

Springer Series in Optical Sciences is led by Editor-in-Chief William T. Rhodes, Georgia Institute of Technology, USA, and provides an expanding selection of research monographs in all major areas of optics:

- lasers and quantum optics
- ultrafast phenomena
- optical spectroscopy techniques
- optoelectronics
- information optics
- applied laser technology
- industrial applications and
- other topics of contemporary interest.

With this broad coverage of topics the series is useful to research scientists and engineers who need up-to-date reference books.

More information about this series at <http://www.springer.com/series/624>

Oleksiy Shulika • Igor Sukhoivanov
Editors

Advanced Lasers

Laser Physics and Technology for Applied
and Fundamental Science

 Springer

Editors

Oleksiy Shulika
Universidad de Guanajuato
Salamanca
Mexico

Igor Sukhoivanov
Universidad de Guanajuato
Salamanca
Mexico

ISSN 0342-4111

ISSN 1556-1534 (electronic)

Springer Series in Optical Sciences

ISBN 978-94-017-9480-0

ISBN 978-94-017-9481-7 (eBook)

DOI 10.1007/978-94-017-9481-7

Library of Congress Control Number: 2014958008

Springer Dordrecht Heidelberg New York London

© Springer Science+Business Media Dordrecht 2015

This work is subject to copyright. All rights are reserved by the Publisher, whether the whole or part of the material is concerned, specifically the rights of translation, reprinting, reuse of illustrations, recitation, broadcasting, reproduction on microfilms or in any other physical way, and transmission or information storage and retrieval, electronic adaptation, computer software, or by similar or dissimilar methodology now known or hereafter developed.

The use of general descriptive names, registered names, trademarks, service marks, etc. in this publication does not imply, even in the absence of a specific statement, that such names are exempt from the relevant protective laws and regulations and therefore free for general use.

The publisher, the authors and the editors are safe to assume that the advice and information in this book are believed to be true and accurate at the date of publication. Neither the publisher nor the authors or the editors give a warranty, express or implied, with respect to the material contained herein or for any errors or omissions that may have been made.

Printed on acid-free paper

Springer is part of Springer Science+Business Media (www.springer.com)

Contents

1	Recent Progress in Polarization-Bistable VCSELs and Their Applications to All-Optical Signal Processing	1
	Hitoshi Kawaguchi	
2	Tunable Lasers Based on Multimode Interference Effects	19
	Daniel A. May-Arrioja, José E. Antonio-Lopez, José J. Sanchez-Mondragón and P. LiKamWa	
3	Whispering Gallery Mode Microdisk Resonator with Dynamic Material Properties	35
	Nataliya Sakhnenko	
4	Superradiant Lasing and Collective Dynamics of Active Centers with Polarization Lifetime Exceeding Photon Lifetime	49
	Vi. V. Kocharovsky, A. A. Belyanin, E. R. Kocharovskaya and V. V. Kocharovsky	
5	The Control of Energy, Temporal and Spatial Characteristics a Microchip Laser with Active Output Mirror	71
	V. V. Kiyko, V. A. Kondratyev, S. V. Gagarsky, E. N. Ofitserov, A. G. Suzdaltsev A. N. Sergeev and V. I. Kislov	
6	Recent Advances in Secure Transmission with Chaotic Carriers	85
	Silvano Donati and Valerio Annovazzi-Lodi	
7	Superwicking Surfaces Produced by Femtosecond Laser	101
	A. Y. Vorobyev and Chunlei Guo	
8	Optical Processors as Conceptual Tools for Designing Nonconventional Devices	117
	Jorge Ojeda-Castañeda, Sergio Ledesma, Emmanuel Yépez-Vidal, Cristina M. Gómez-Sarabia and Miguel Torres-Cisneros	

9	Description of the Dynamics of Charged Particles in Electric Fields: An Approach Using Fractional Calculus	147
	F. Gómez-Aguilar and E. Alvarado-Méndez	
10	Sub- and Nanosecond Pulsed Lasers Applied to the Generation of Broad Spectrum in Standard and Microstructured Optical Fibers	159
	Julián M. Estudillo-Ayala, Roberto Rojas-Laguna, Juan C. Hernández García, Daniel Jauregui-Vazquez and Juan M. Sierra Hernandez	
11	Extremely High Power CO₂ Laser Beam Correction	173
	Alexis Kudryashov, Alexander Alexandrov, Alexey Rukosuev and Vadim Samarkin	
12	Measurements of Intense and Wide-Aperture Laser Radiation Parameters with Thinwire Bolometers	183
	S. V. Pogorelov	
13	Spectral and Lasing Characteristics of Some Red and Nir Laser Dyes in Silica Matrices	199
	I. M. Pritula, O. N. Bezkrovnaya, V. M. Puzikov, V. V. Maslov, A. G. Plaksey, A. V. Lopin and Yu. A. Gurkalenko	
14	Interpretation of the Time Delay in the Ionization of Coulomb Systems by Attosecond Laser Pulses	213
	Vladislav V. Serov, Vladimir L. Derbov and Tatyana A. Sergeeva	
	Index	231

Contributors

Alexander Alexandrov Adaptive Optics Lab, Moscow State Technical University (MAMI), Moscow, Russia

E. Alvarado-Méndez Departamento de Ingeniería Electrónica, División de Ingenierías Campus Irapuato Salamanca, Universidad de Guanajuato, Salamanca, GTO, México

Valerio Annovazzi-Lodi Department of Electrical, Computer and Biomedical Engineering, University of Pavia, Pavia, Italy

José E. Antonio-Lopez CREOL The College of Optics and Photonics, University of Central Florida, Orlando, FL, USA

A. A. Belyanin Department of Physics and Astronomy, Texas A & M University, College Station TX, USA

O. N. Bezkravnaya Institute for Single Crystals, SSI “Institute for Single Crystals”, National Academy of Sciences of Ukraine, Kharkiv, Ukraine

Vladimir L. Derbov Department of Physics, Saratov State University, Saratov, Russia

Silvano Donati Department of Electrical, Computer and Biomedical Engineering, University of Pavia, Pavia, Italy

Julián M. Estudillo-Ayala Cuerpo Académico de Optoelectrónica, DICIS Universidad de Guanajuato, Guanajuato, Mexico

F. Gómez-Aguilar Departamento de Materiales Solares, Instituto de Energías Renovables, Universidad Nacional Autónoma de México, Temixco, MOR, México

Cristina M. Gómez-Sarabia Digital Arts Department, Engineering Division, Campus Salamanca, University of Guanajuato, Guanajuato, Mexico

S. V. Gagarsky Mechanics and Optics, Saint Petersburg National Research University of Information Technologies, Saint-Petersburg, Russia

Chunlei Guo The Institute of Optics, University of Rochester, Rochester, NY, USA

Yu. A. Gurkalenko Institute for Single Crystals, SSI “Institute for Single Crystals”, National Academy of Sciences of Ukraine, Kharkiv, Ukraine

Juan C. Hernandez Garcia Instituto Nacional de Astrofísica Óptica y Electrónica, Puebla, Mexico

Daniel Jauregui-Vazquez Cuerpo Académico de Optoelectrónica, DICIS Universidad de Guanajuato, Guanajuato, Mexico

Hitoshi Kawaguchi Graduate School of Materials Science, Nara Institute of Science and Technology, Ikoma, Nara, Japan

V. I. Kislov Prokhorov General Physics Institute, Russian Academy of Science, Moscow, Russia

V. V. Kiyko Prokhorov General Physics Institute, Russian Academy of Science, Moscow, Russia

E. R. Kocharovskaya IAP RAS, Nizhny Novgorod, Russia

V. V. Kocharovsky IAP RAS, Nizhny Novgorod, Russia

Department of Physics and Astronomy, Texas A & M University, College Station TX, USA

VI. V. Kocharovsky IAP RAS, Nizhny Novgorod, Russia

V. A. Kondratyev Prokhorov General Physics Institute, Russian Academy of Science, Moscow, Russia

Alexis Kudryashov Adaptive Optics Lab, Moscow State Technical University (MAMI), Moscow, Russia

Sergio Ledesma Electronics Department, Engineering Division, Campus Salamanca, University of Guanajuato, Guanajuato, Mexico

P. LiKamWa CREOL The College of Optics and Photonics, University of Central Florida, Orlando, FL, USA

A. V. Lopin Institute for Single Crystals, SSI “Institute for Single Crystals”, National Academy of Sciences of Ukraine, Kharkiv, Ukraine

V. V. Maslov O. Ya. Usikov Institute for Radiophysics and Electronics, National Academy of Sciences of Ukraine, Kharkiv, Ukraine

Daniel A. May-Arrijo Fiber and Integrated Optics Laboratory, UAMRR Universidad Autónoma de Tamaulipas, Reynosa, TAMPAS, México

E. N. Ofitserov Prokhorov General Physics Institute, Russian Academy of Science, Moscow, Russia

Jorge Ojeda-Castañeda Electronics Department, Engineering Division, Campus Salamanca, University of Guanajuato, Guanajuato, Mexico

A. G. Plaksiy Institute for Single Crystals, SSI “Institute for Single Crystals”, National Academy of Sciences of Ukraine, Kharkiv, Ukraine

S. V. Pogorelov National University of Pharmacy, Kharkov, Ukraine

I. M. Pritula Institute for Single Crystals, SSI “Institute for Single Crystals”, National Academy of Sciences of Ukraine, Kharkiv, Ukraine

V. M. Puzikov Institute for Single Crystals, SSI “Institute for Single Crystals”, National Academy of Sciences of Ukraine, Kharkiv, Ukraine

Roberto Rojas-Laguna Cuerpo Académico de Optoelectrónica, DICIS Universidad de Guanajuato, Guanajuato, Mexico

Alexey Rukosuev Adaptive Optics Lab, Moscow State Technical University (MAMI), Moscow, Russia

Nataliya Sakhnenko Kharkiv National University of Radio Electronics, Kharkiv, Ukraine

Institute of Radio Physics and Electronics NASU, Kharkiv, Ukraine

Vadim Samarkin Adaptive Optics Lab, Moscow State Technical University (MAMI), Moscow, Russia

José J. Sanchez-Mondragón Instituto Nacional de Astrofísica, Óptica y Electrónica, Tonantzintla, PUE, México

A. N. Sergeev Mechanics and Optics, Saint Petersburg National Research University of Information Technologies, Saint-Petersburg, Russia

Tatyana A. Sergeeva Department of Physics, Saratov State University, Saratov, Russia

Vladislav V. Serov Department of Physics, Saratov State University, Saratov, Russia

Juan M. Sierra Hernandez Cuerpo Académico de Optoelectrónica, DICIS Universidad de Guanajuato, Guanajuato, Mexico

A. G. Suzdaltsev Prokhorov General Physics Institute, Russian Academy of Science, Moscow, Russia

Miguel Torres-Cisneros Electronics Department, Engineering Division, Campus Salamanca, University of Guanajuato, Guanajuato, Mexico

A. Y. Vorobyev The Institute of Optics, University of Rochester, Rochester, NY, USA

Emmanuel Yépez-Vidal Electronics Department, Engineering Division, Campus Salamanca, University of Guanajuato, Guanajuato, Mexico

Chapter 8

Optical Processors as Conceptual Tools for Designing Nonconventional Devices

Jorge Ojeda-Castañeda, Sergio Ledesma, Emmanuel Yépez-Vidal,
Cristina M. Gómez-Sarabia and Miguel Torres-Cisneros

Abstract We discuss the use of nonconventional optical processors for generating irradiance distributions, which are useful for visualizing the characteristics of imaging devices that extend the depth of field. Our discussion starts with the use of binary masks for generating nonconventional irradiance distributions, which display the variations of the impulse response with focus errors. By using an anamorphic optical processor these irradiance distributions can easily be transformed into variations of the optical transfer function vs focus errors. Next, another anamorphic optical processor is used for generating the ambiguity function of a pupil aperture, which helps to visualize the variations of the optical transfer function with variable focus error. Finally, we translate the integral transform associated with the evaluation of the ambiguity function into tunable devices for controlling the depth of field, without modifying the size of the pupil aperture.

8.1 Introduction

In image science, the word apodization is used for describing a large set of techniques for shaping the Point Spread Function (PSF) of an optical system. However, the word apodization [1–6] was coined in optical spectroscopy for describing the use of tapered 1-D pupil masks that reduce diffraction bands, or optical side lobes, on the PSF. It was recognized that this type of tapering masks also expand the width of the PSF, while reducing the presence of the side lobes. These two previous features are useful for extending the axial PSF of a 2-D, radially symmetric optical systems [7–9]. For this type of applications, it is convenient to recognize that the normalized version of the axial PSF expresses the Strehl ratio vs focus error [10].

J. Ojeda-Castañeda (✉) · S. Ledesma · E. Y.-Vidal · M. T.-Cisneros
Electronics Department, Engineering Division, Campus Salamanca, University of Guanajuato,
Guanajuato, Mexico
e-mail: jojedacas@ugto.mx

C. M. Gomez-Sarabia
Digital Arts Department, Engineering Division, Campus Salamanca,
University of Guanajuato, Guanajuato, Mexico

Of course, one can extend the depth of field of an imaging device, simply by closing down the pupil aperture or by using annular pupil apertures. However, these solutions reduce the resolution as well as the light gathering power of the optical system. Hence, there is an optical engineering endeavor that aims to reduce the influence of focus errors on the optical transfer function (OTF), without substantially reducing either the resolution or the light gathering power of an optical system [11–14].

In Sect. 8.2, we discuss the use of binary masks that have unit transmittance only along a very narrow slit, which follows suitable paths for generating optical path differences [15–18].

In Sect. 8.3, we show that a display of the ambiguity function [19–23] is rather useful diagram for visualizing the impact of focus error on the OTF. The ambiguity function of the pupil aperture exhibits (in a single picture) the influence of focus error on the OTF. Furthermore, the ambiguity function helps to expand the defocused OTF as a Taylor series expansion in terms of the focus error coefficient. Half of the terms of the Taylor series can be reduced to zero if the complex amplitude transmittance of the pupil aperture is a hermitian function. Hence, one needs to explore the use of masks whose amplitude variations are described by even functions, while the phase variations are described by odd functions [24].

By using a suitable mask one can obtain an OTF that does not have zero values inside the passband, and the OTF varies slowly with focus errors. Thus, one can preserve the spatial frequency content of several planar images, which are located at different depths. These images are recorded with virtually the same amount of contrast reduction. Consequently, one can use the same digital filter for restoring the contrast of all recorded images [25].

The present technology allows producing nonconventional masks, with complex amplitude transmittance. Furthermore, there several fast digital algorithms for improving the quality of an image. Hence, nowadays one can use both nonconventional devices with complex amplitude transmittance, as well as fast digital algorithms for extending the depth of field [26–31].

In Sect. 8.4, we show that the schematics of an optical processor are useful for gaining physical insights, on the design of tunable devices for controlling the depth of field. To this end, we translate the integral transform associated with the evaluation of the ambiguity function into tunable devices for controlling the depth of field, without modifying the pupil aperture. These types of devices are here denoted as Alvarez-Lohmann lenses. In Sect. 8.5, we summarize our contribution.

8.2 Visualizing a PSF with High Depth of Focus

We start by writing Helmholtz differential equation that describes the propagation of a 2-D scalar wave $\varphi(x, z)$. That is,

$$[\partial_x^2 + \partial_z^2 + k^2]\varphi(x, z) = 0. \quad (8.1)$$

In Eq. (8.1) the wave number is denoted as $k = 2\pi/\lambda$. It is easy to verify that its formal solution is

$$\varphi(x, z) = \exp \left[ikz \sqrt{k^{-2} \partial_x^2 + 1} \right] \varphi(x, 0). \quad (8.2)$$

The exponential operator in Eq. (8.2) is to be used as a power series expansion of the differential operator ∂_x^2 . See for example references from 32 to 34. One can relate the formal solution in Eq. (8.2) to the angular spectrum of plane waves, by assuming that the initial condition $\varphi(x, z = 0)$ can be expressed as the inverse Fourier transform of the plane wave spectrum $\Phi(\mu)$. That is,

$$\varphi(x, 0) = \int_{-\infty}^{\infty} \Phi(\mu) \exp(i 2\pi x \mu) d\mu \quad (8.3)$$

In Eq. (8.3) we use the Greek letter μ for denoting the spatial frequency along the horizontal axis, which is of course related to direction cosine along the horizontal axis α as follows, $\mu = \alpha/\lambda$. If one applies the exponential operator in Eq. (8.2) to the inverse Fourier transform in Eq. (8.3) one obtains

$$\begin{aligned} & \exp \left[ikz \sqrt{k^{-2} \partial_x^2 + 1} \right] \varphi(x, 0) \\ &= \int_{-\infty}^{\infty} \Phi(\mu) \exp[ikz \sqrt{1 - \lambda^2 \mu^2}] \exp(i 2\pi x \mu) d\mu. \end{aligned} \quad (8.4)$$

As one should expect. The result in Eq. (8.4) can be usefully rewritten in the following manner. As is depicted in Fig. 8.1, let us assume that in a classical optical processor the input is a pinhole size source, which is represented by the mathematical expression

$$u_0(x, z) = \delta(x) \delta(z). \quad (8.5)$$

As is depicted in Fig. 8.1, at the Fraunhofer plane with spatial frequency variables (μ, ζ) , we place a mask with complex amplitude transmittance

$$P(\mu, \zeta) = Q(\mu) \delta(\zeta - \sqrt{\Omega^2 - \mu^2}). \quad (8.6)$$

At this stage, we set $Q(\mu) = \text{rect}(\mu/2\Omega)$ where the Greek letter Ω denotes the cut-off value of the spatial frequency μ . The second term in Eq. (8.6) describes a very narrow slit that follows the curve $\zeta = \sqrt{\Omega^2 - \mu^2}$. The amplitude impulse response of the coherent optical processor is

$$p(x, z) = \int_{-\infty}^{\infty} \int_{-\infty}^{\infty} P(\mu, \zeta) \exp[i 2\pi (x\mu + z\zeta)] d\mu d\zeta \quad (8.7a)$$

Or equivalently, by using Eq. (8.6), one can write Eq. (8.7a) as

$$p(x, z) = \int_{-\infty}^{\infty} Q(\mu) \exp[i 2\pi (x\mu + z\sqrt{\Omega^2 - \mu^2})] d\mu \quad (8.7b)$$

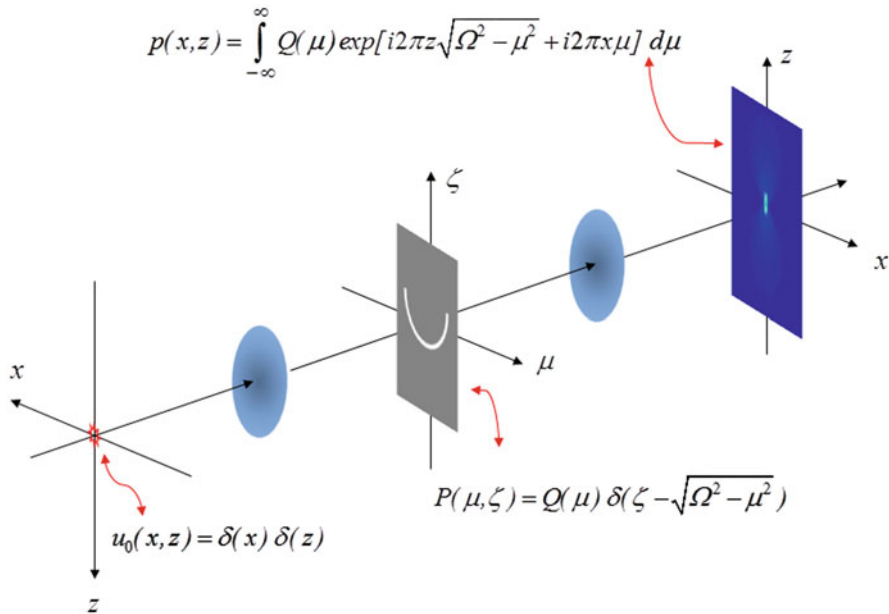


Fig. 8.1 Schematic diagram of an optical processor using a pupil mask in the form of narrow slit

By a simple comparison, between Eqs. (8.4) and (8.7b), it is apparent that the optical processor is able to display, in a single 2-D picture, the propagation the scalar wave $\phi(x, z)$; where $\Omega = \lambda^{-1}$.

One can generalize this remarkably simple result by selecting the complex amplitude distribution, at the Fraunhofer plane, as

$$Q(\mu) = \Phi(\mu) \text{rect}\left(\frac{\mu}{2\lambda^{-1}}\right). \quad (8.8)$$

We discuss next other useful examples. In the paraxial regime, the propagation of a 2-D wave scalar wave $\phi(x, z)$ can be is described using the differential equation

$$[\partial_x^2 + i2k\partial_z] \phi(x, z) = 0 \quad (8.9)$$

It is straightforward to show that for this case, as depicted in Fig. 8.2, on needs a mask with complex amplitude transmittance

$$P(\mu, \zeta) = Q(\mu) \delta\left(\zeta + \frac{\mu^2}{2\Omega}\right); \quad (8.10)$$

where again $\Omega = \lambda^{-1}$. In Fig. 8.3 we show the irradiance distributions associated to the pictures describing the propagation of an initial point source, as predicted by Helmholtz equation; as well as the picture that portraits wave propagation within the paraxial approximation. It is interesting to note that the picture describing propagation in the paraxial regime (left hand side of Fig. 8.3) has a wider diverging angle

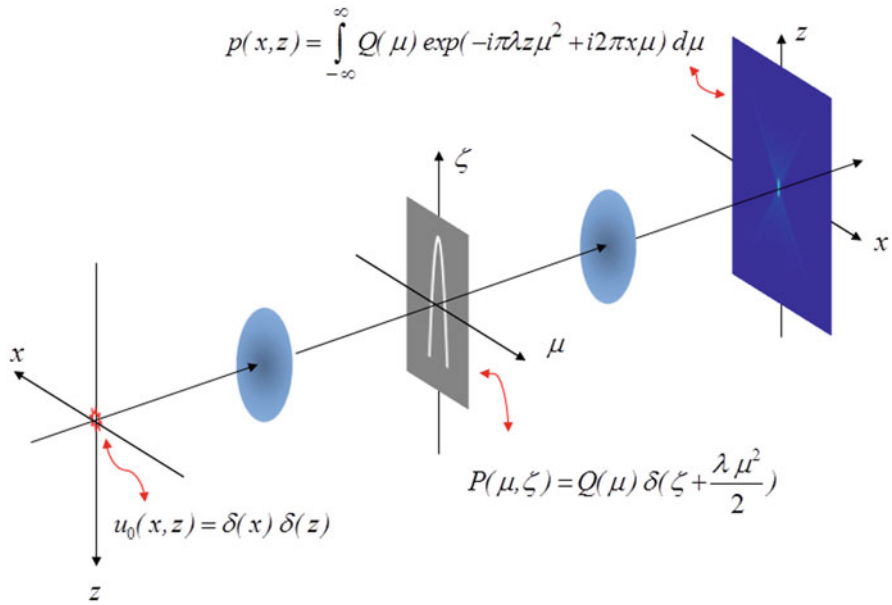


Fig. 8.2 Optical processor used for visualizing the propagation of a 2-D scalar wave, in the paraxial regime

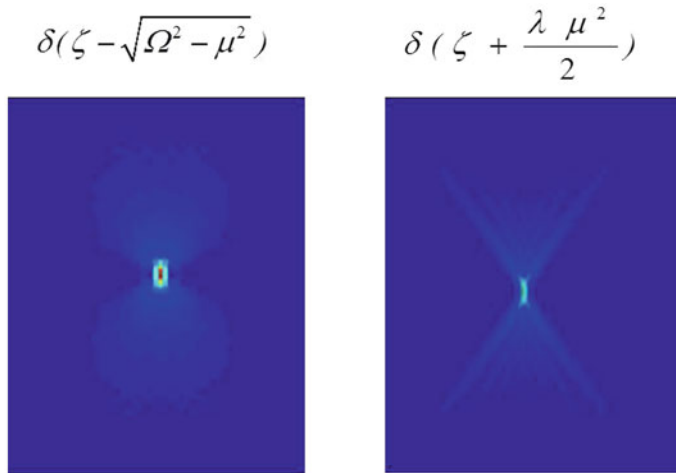


Fig. 8.3 Irradiance distributions displaying the impulse response at the (x, z) plane

than the picture describing propagation according to Helmholtz equation (right hand side of Fig. 8.3).

Next, we discuss an interesting variant of our previous results. As depicted in Fig. 8.4, let us assume that the mask has the following complex amplitude transmittance

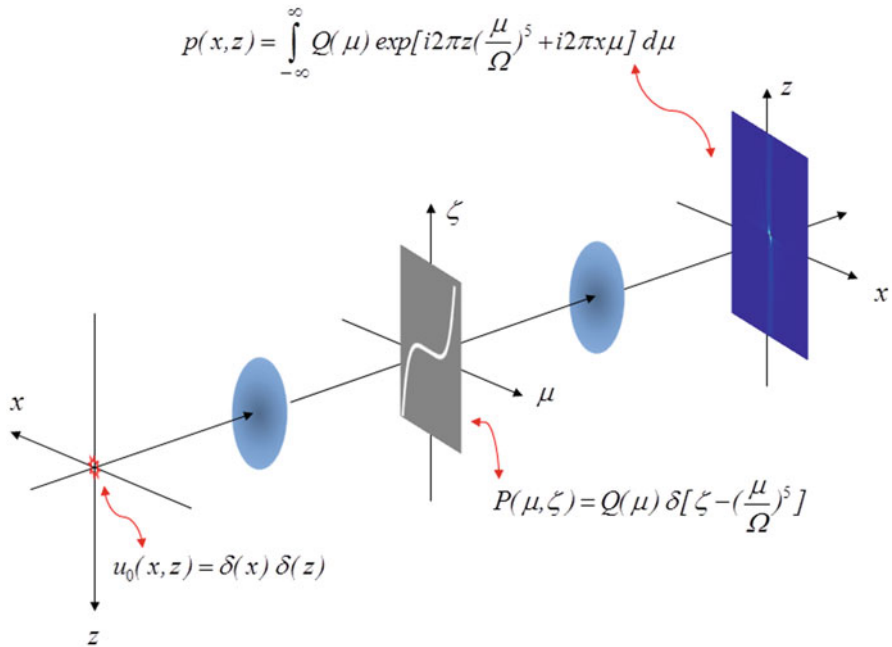


Fig. 8.4 Optical processor using a pupil mask in the form of narrow slit, which follows a fifth power curve

$$P(\mu, \zeta) = Q(\mu) \delta \left[\zeta - \sigma \left(\frac{\mu}{\Omega} \right)^5 \right]. \quad (8.11)$$

At the output plane of the coherent optical processor, the complex amplitude distribution is

$$p(x, z) = \int_{-\infty}^{\infty} Q(\mu) \exp \left\{ i2\pi \left[x\mu + z\sigma \left(\frac{\mu}{\Omega} \right)^5 \right] \right\} d\mu. \quad (8.12)$$

The complex amplitude distribution in Eqs. (8.11) and (8.12) have now the following interpretation.

At the Fraunhofer plane the curve $\zeta = (\mu/\Omega)^5$ represents a phase profile to the fifth power. Hence, now at the output plane, the z -axis denotes the maximum value of the optical path difference, which is reached at the edge ($\mu = \pm \Omega$) of the 1-D pupil aperture. Again the pupil aperture is described by the function $\text{rect}(\mu/2\Omega)$. Consequently, in this later example, the variable ζ is a dimensionless variable. Its Fourier transform pair is the dimensionless variable

$$z = (N - 1) \frac{t}{\lambda} \quad (8.13)$$

Table 8.1 Possible curve for the narrow slit in the Fraunhofer plane. The displays that are described along the third column are obtained using the optical processor in Fig. 8.1. And the displays along the third column are obtained using the optical processor in Fig. 8.6.

Describing	Binary Mask	Display 1	Display 2
Nonparaxial propagation	$P(\mu, \zeta) = Q(\mu)\delta(\zeta - \sqrt{\Omega^2 - \mu^2})$	PSF along the Z-axis	MTF along the Z-axis
Paraxial propagation	$P(\mu, \zeta) = Q(\mu)\delta\left(\zeta + \frac{\mu^2}{2\Omega}\right)$	PSF along the Z-axis	MTF along the Z-axis
Asymmetric quadratic phase mask	$P(\mu, \zeta) = Q(\mu)\delta\left[\zeta - \text{sgn}(\mu)\left(\frac{\mu}{\Omega}\right)^2\right]$	PSF vs OPD	MTF vs OPD
Cubic phase mask	$P(\mu, \zeta) = Q(\mu)\delta\left[\zeta - \left(\frac{\mu}{\Omega}\right)^3\right]$	PSF vs OPD	MTF vs OPD
Fractional wavefront	$P(\mu, \zeta) = Q(\mu)\delta\left[\zeta - \text{sgn}(\mu)\left \frac{\mu}{\Omega}\right ^{3.75}\right]$	PSF vs OPD	MTF vs OPD
High order phase mask	$P(\mu, \zeta) = Q(\mu)\delta\left[\zeta - \left(\frac{\mu}{\Omega}\right)^5\right]$	PSF vs OPD	MTF vs OPD

Hence, as is indicated in Eq. (8.13), the Latin letter z describes the variation of optical path difference of an optical element. We denote with the letter N the refractive index, and we assume that the optical element is surrounded by air, and that it has a physical thickness t .

A similar interpretation can be applied to other narrow slits that follow other curves in the Fraunhofer domain, namely

$$P(\mu, \zeta) = Q(\mu)\delta\left[\zeta - \sigma\left|\frac{\mu}{\Omega}\right|^m\right]. \quad (8.14)$$

In Eq. (8.14) the Latin letter m is a real number that indicates power of the monomial μ/Ω . At the output plane of the coherent optical processor, in Fig. 8.3, the complex amplitude distribution displays the changes of the coherent impulse response in terms of the position variable x , as well as in terms of the dimensionless variable z , which represents the variations of optical path difference caused by a refractive optical element; as is indicated in Eq. (8.13).

In Table 8.1 we summarize other possible options when selecting the curve that the narrow slit must follow in the Fraunhofer domain. It is to be noted by using this procedure one can visualize the impact of optical path difference on the behavior of the impulse response for rather unconventional phase delays; as indicated in Fig. 8.5. From this latter figure, it is apparent the unique behavior of the phase mask with fractional power phase profile. Otherwise, we note that the selected phase masks generate asymmetric irradiance distributions, which spread out as the optical path difference increases.

In Fig. 8.6, we show the schematics of an anamorphic optical processor. Now, for the new optical processor, the input is the irradiance distribution that is obtained at the output plane of the previous optical processor. As is apparent from the schematic

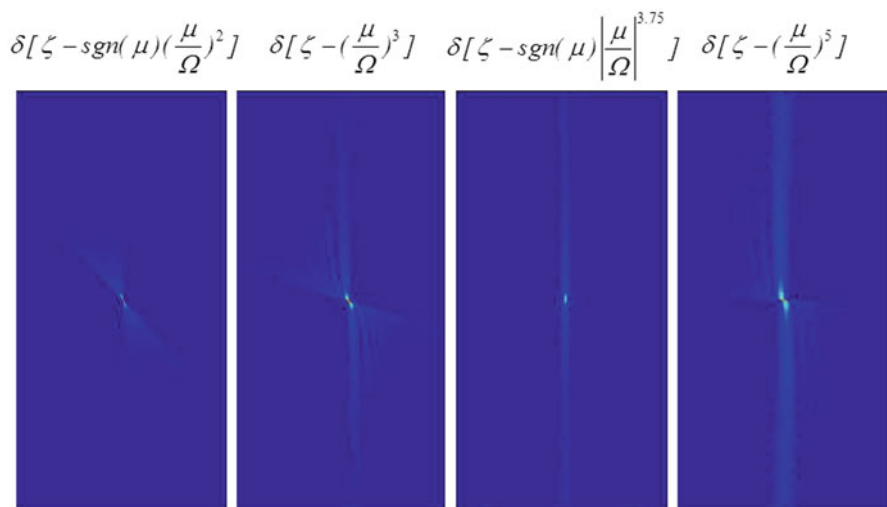


Fig. 8.5 Impulse response as a function of the position and of the optical path difference of several nonconventional optical elements

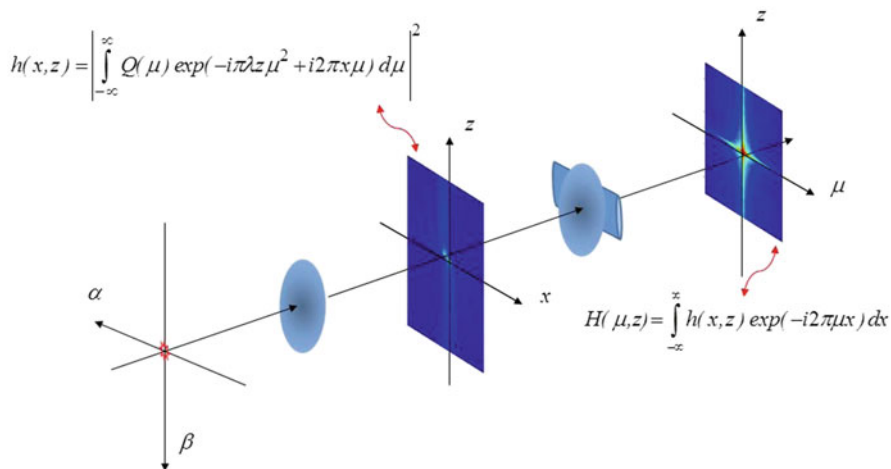


Fig. 8.6 Anamorphic optical processor for displaying (as irradiance variations) the OTF's of several optical elements

diagram in Fig. 8.6, the new anamorphic optical processor implements an imaging operation, with magnification equals to unity, along the vertical axis while it implements a Fourier transformation along the horizontal axis. That is, at the output plane of the new optical processor, the complex amplitude distribution is

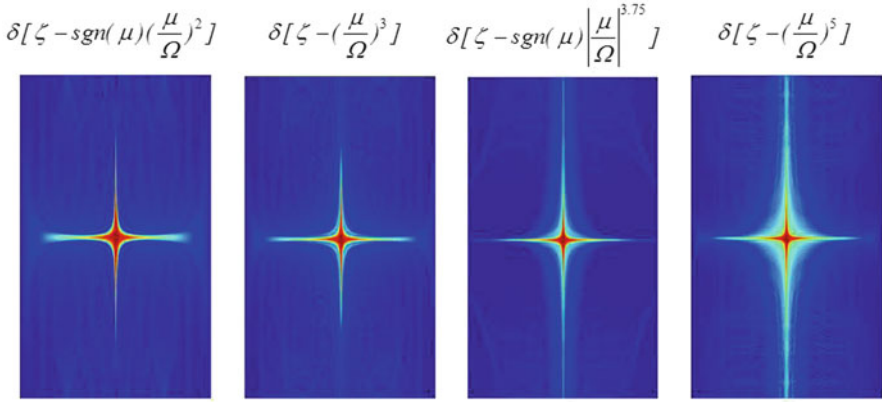


Fig. 8.7 Variations of the MTF as a function of the spatial frequency μ (*horizontal axis*) as well as a function of the optical path difference (*vertical axis*) for four different phase profiles

$$\begin{aligned}
 H(\mu, z) &= \int_{-\infty}^{\infty} \int_{-\infty}^{\infty} |p(x, z')|^2 \exp(-i2\pi\mu x) \delta(z - z') dx dz' \\
 &= \int_{-\infty}^{\infty} |p(x, z)|^2 \exp(-i2\pi\mu x) dx.
 \end{aligned} \tag{8.15}$$

The result in Eq. (8.15) indicates the following. At the output plane of the anamorphic optical processor in Fig. 8.6, one can obtain optically a complex amplitude distribution that is proportional to the Optical Transfer Function (OTF) as a function of both the spatial frequency μ and the axial distance z .

Of course, when visualizing the OTF one uses a square law detector for obtaining the square modulus of the OTF. Hence, the irradiance distribution at the output is the square value of the Modulation Transfer Function (MTF).

In Fig. 8.7 we show the display of the MTF's that are obtained when using, respectively, the curve $\zeta = \text{sgn}(\mu) (\mu/\Omega)^2$, as well as the curves that are described along the lines 3, 4 and 5 in Table 8.1. It is apparent from Fig. 8.7 that as the optical path difference increases, the MTF's tend to spread out. However, the MTF's exhibit spurious oscillations. It is clear from Fig. 8.7 that again the phase mask with phase profile with fractional power ($m = 3.75$) has reduced spurious oscillations. In the following section, while we describe another method for visualizing the impact of focus error on the MTF, we discuss an optical technique that strongly reduces the spurious oscillations on the MTF.

Several years ago, some of us established a link between the OTF suffering from focus errors and the ambiguity function of the pupil aperture [23]. Later on, the ambiguity function was applied as a mathematical tool for proposing optical masks that reduce the impact of focus error on the OTF [35].

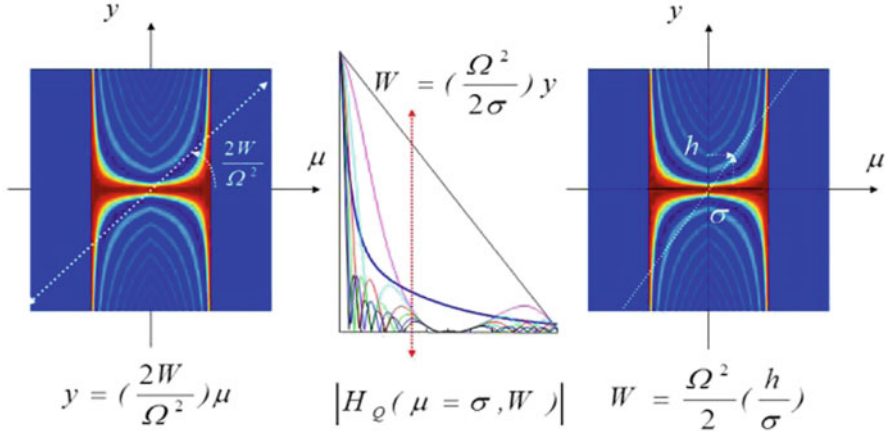


Fig. 8.9 Scanning lines along the ambiguity function for obtaining the values of the out-of-focus MTF

As is well known, the OTF of Eq. (8.16) is

$$H_Q(\mu; W) = N_{orma} \int_{-\infty}^{\infty} P\left(v + \frac{\mu}{2}\right) P^*\left(v - \frac{\mu}{2}\right) dv$$

$$H_Q(\mu; W) = N_{orma} \int_{-\infty}^{\infty} Q\left(v + \frac{\mu}{2}\right) Q^*\left(v - \frac{\mu}{2}\right) \exp\left[i2\pi\left(\frac{2W\mu}{\Omega^2}\right)v\right] dv. \quad (8.18)$$

In Eq. (8.18) the upper case letter N_{orma} denotes a suitable normalization factor. On the other hand, the ambiguity function of the pupil mask, $Q(\mu)$, is

$$A_Q(\mu, y) = N_{orma} \int_{-\infty}^{\infty} Q\left(v + \frac{\mu}{2}\right) Q^*\left(v - \frac{\mu}{2}\right) \exp[i2\pi y v] dv. \quad (8.19)$$

From a simple comparison between Eqs. (8.18) and (8.19), we note that

$$y = \left(\frac{2W}{\Omega^2}\right) \mu. \quad (8.20)$$

If in the display of the ambiguity function (as that at the left hand-side of Fig. 8.9) one traces a straight-line, crossing the origin; the slope is proportional to the amount of focus error; as indicated in Eq. (8.20). If one selects a value of the spatial frequency, say $\mu = \sigma$, then the variations of the OTF for variable focus errors can be visualized by moving up or down along a vertical line; as depicted at the centre of Fig. 8.9. Furthermore, for a given position along the vertical line, say $y = h$, the focus error coefficient is $W = (\Omega^2/2) (h/\sigma)$.

Next, we recognize that for displaying the ambiguity function, one can use the anamorphic processor in Fig. 8.10. See for example reference [36]. In Fig. 8.10, we

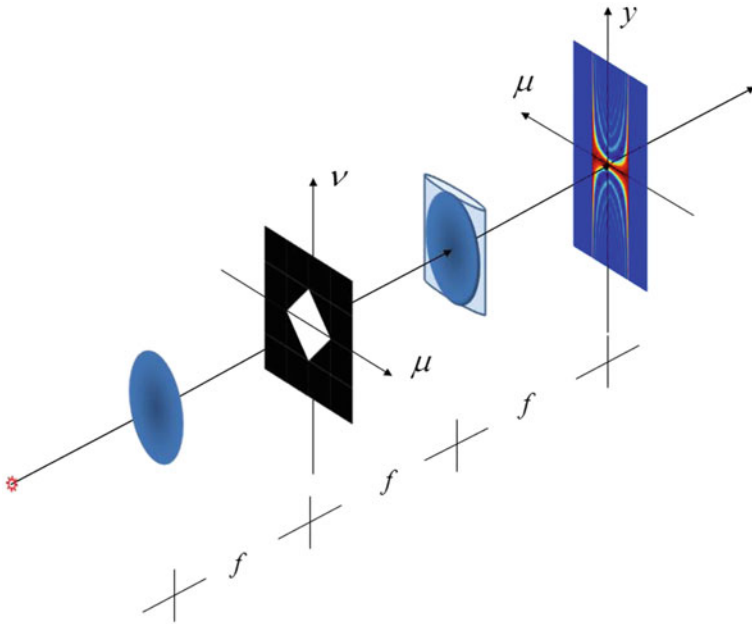


Fig. 8.10 Anamorphic optical processor that is used for visualizing the Ambiguity function

indicate that the input for the anamorphic processor is the *Product Spectrum*, which is

$$P_Q(\mu, \nu) = Q\left(\nu + \frac{\mu}{2}\right) Q^*\left(\nu - \frac{\mu}{2}\right). \quad (8.21)$$

For a clear pupil aperture, $Q(\mu) = \text{rect}(\mu/2\Omega)$ then the Product Spectrum is

$$P(\mu, \nu) = \text{rect}\left(\frac{\mu}{4\Omega}\right) \text{rect}\left(\frac{\nu}{2\Omega - |\mu|}\right). \quad (8.22)$$

We note that the anamorphic processor, in Fig. 8.10, performs an imaging operation, with unit magnification, along the horizontal axis. From Fig. 8.10 and Eq. (8.22) the following considerations are apparent. Inside the passband, $|\mu| \leq 2\Omega$, a vertical line along the product spectrum is bounded by the function $\text{rect}[\nu/(2\Omega - |\mu|)]$.

Hence, at the output plane of the optical processor, along the vertical axis one has the Fraunhofer diffraction pattern of a rectangular window. Thus, at the output plane of the optical processor, the complex amplitude distribution is

$$A_Q(\mu, y) = \left(1 - \frac{|\mu|}{2\Omega}\right) \text{sinc}\left[\left(1 - \frac{|\mu|}{2\Omega}\right)y\right] \quad (8.23)$$

In other words, the ambiguity function is composed by a series of sinc functions with variable half-width. Consequently, the out-of-focus OTF exhibits a large number of

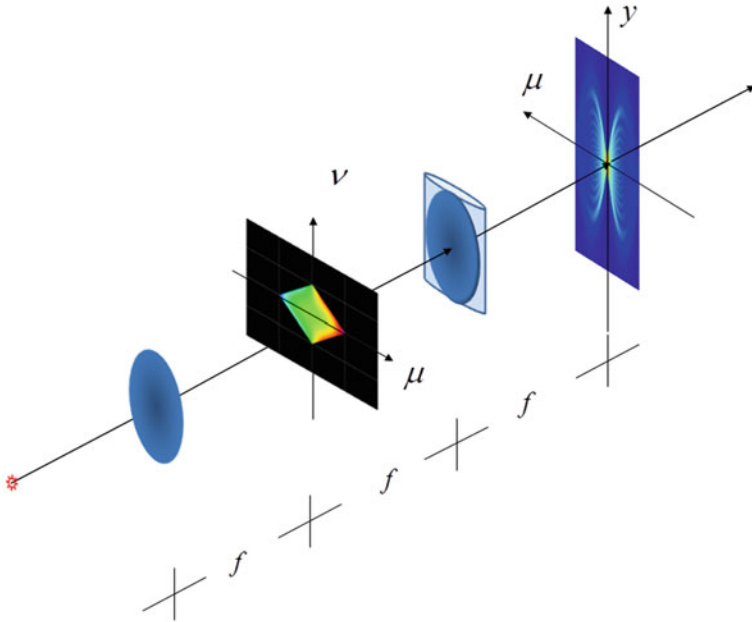


Fig. 8.11 Use of phase-only masks for obtaining ambiguity functions with “Bow-Tie” effect

zero crossings. If one wants to modify this result, then one needs to consider another possible ambiguity functions. For example, if at the **Product spectrum** we have a vertical line that has a quadratic phase factor,

$$P(\mu, v) = \exp \left[i2\pi a \left(\frac{v}{\Omega} \right)^2 \right] \text{rect} \left[\frac{v}{2\Omega - |\mu|} \right] \text{rect} \left[\frac{\mu}{4\Omega} \right]. \quad (8.24)$$

For obtaining this type of **Product Spectrum**, one needs a cubic phase mask, as proposed by Dowski and Cathey. If, as depicted in Fig. 8.11, now we take the complex amplitude transmittance along a vertical line vertical axis, and we evaluate the Fourier transform of Eq. (8.24), we obtain

$$A_Q(\mu, y) = \text{rect} \left(\frac{\mu}{4\Omega} \right) \int_{-\frac{(2\Omega-|\mu|)}{2}}^{\frac{(2\Omega-|\mu|)}{2}} \exp \left\{ i2\pi \left[a \left(\frac{\mu}{\Omega} \right)^2 + yv \right] \right\} dv. \quad (8.25)$$

It is apparent from Eq. (8.25) that along the y -axis, the ambiguity function results from the lateral superposition of Fresnel diffraction patterns of rectangular windows, which have variable width. See Fig. 8.11.

Since any vertical line is a Fresnel diffraction pattern, then the ambiguity function spreads all over the (μ, y) plane. This behaviour is known as the “bow-tie effect”.

See reference [37]. As a consequence, the OTF's have low sensitivity to focus errors. Of course, one can extrapolate this previous result, by exploring the use of high order aberration polynomials. That is,

$$Q(\mu) = \exp \left\{ i2\pi a \left(\frac{\mu}{\Omega} \right)^{2m+1} \right\} \text{rect} \left(\frac{\mu}{2\Omega} \right). \quad (8.26)$$

One can guess that the phase mask described in Eq. (8.26) will be able to spread the ambiguity function along the vertical axis; as is depicted in Fig. 8.11. Consequently, one expects that this type of masks will be able to extend the depth of field. However, it is relevant to note that these types of high order phase masks (including the cubic phase mask) introduce spurious oscillations. For reducing this undesirable feature, one can use a Gaussian apodizer on the pupil aperture; as part of the spatial filter. In other words, now the complex amplitude transmittance of the pupil aperture is

$$Q(\mu) = \exp \left\{ i2\pi a \left(\frac{\mu}{\Omega} \right)^{2m+1} - c \left(\frac{\mu}{\Omega} \right)^2 \right\} \text{rect} \left(\frac{\mu}{2\Omega} \right). \quad (8.27)$$

In Eq. (8.27) the lower case letter “c” denotes a damping factor, in the amplitude variations, which are described by a Gaussian profile. See reference [38].

At the top of Fig. 8.12, we show the MTF of a cubic phase mask for $W = 0$ and for $W = 3$. One can note that there are spurious oscillations. At the bottom of Fig. 8.12, we show the MTF that is obtained if one use the complex amplitude transmittance in Eq. (8.27) for $m = 1$. From the results at the bottom of Fig. 8.12, it is apparent that a Gaussian apodizer is able to reduce unwanted oscillations in the MTF; without spoiling the low sensitivity of the MTF to focus errors.

The tapering mask with Gaussian profile has the following additional advantages, which are illustrated in Fig. 8.13. First, by using a Gaussian apodizer the 2-D rectangular pupil aperture is transformed into a nearly circularly symmetric aperture; as is indicated along the first column of Fig. 8.13.

Furthermore, the Gaussian apodizer reduces the diffraction lobes in the asymmetric PSF; as depicted along the second column of Fig. 8.13. We note also that the Gaussian apodizer broadens the MTF, as shown along the third column of Fig. 8.13. The above results can also be visualized in terms of the product spectrum and the ambiguity function; as we depict next.

Along the first column in Fig. 8.14, we show the influence that a Gaussian mask has on the product spectrum. Along the second column, first line, in Fig. 8.14 we display zero-phase variations inside the support of the product spectrum. Along the second column, line two, of Fig. 8.14 we show as colour variations the profile of a 2-D cubic phase mask. And along the second column, line three, in Fig. 8.14 we show the phase delays of a 2-D cubic phase mask.

From the third column in Fig. 8.14 the following characteristics are apparent. Along the first line and third column of Fig. 8.14, we have that the modulus of the ambiguity function has several regions with zero values. Then as depicted in the second line and third column of Fig. 8.14, if one uses a cubic phase masks the modulus of the ambiguity function has extended regions with nonzero values. However, the

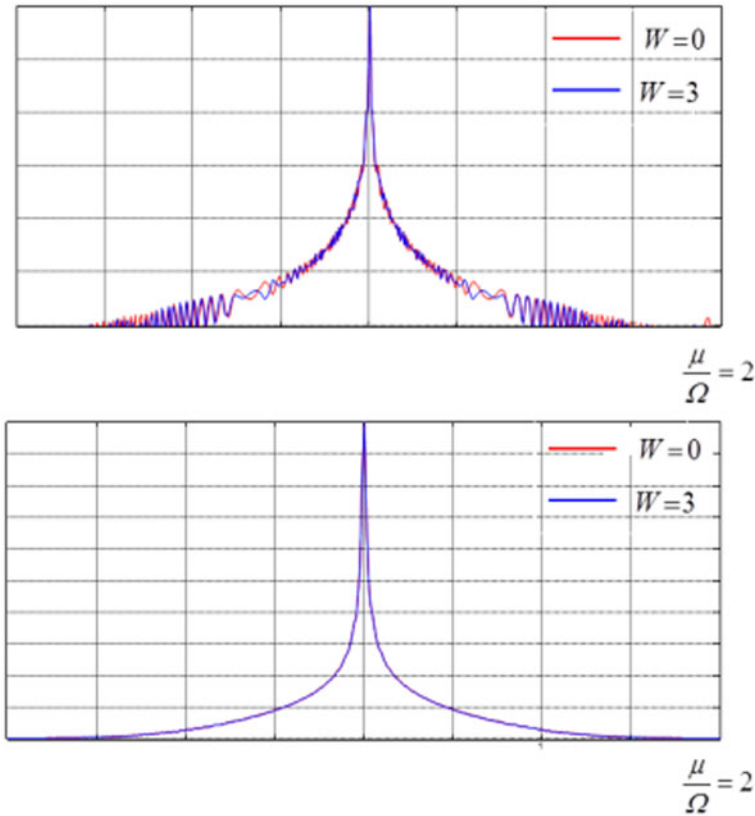


Fig. 8.12 Use of a Gaussian mask for reducing the spurious oscillations on the in-focus MTF and out-of-focus MTF

nonzero values have spurious oscillations. Finally, as shown in the second line and third column of Fig. 8.14, if one uses a Gaussian mask together with a cubic phase masks one can reduce the spurious oscillations on the regions with nonzero values.

For obtaining the numerical simulations in Fig. 8.14, which are described by Eq. (8.27), we select the values $a = 33$, $n = 1$ and $c = 0.44$. These results are generalized in reference [39], where we use the following definition for hyper Gaussian masks. In what follows we consider that the complex amplitude transmittance of the pupil aperture is

$$Q(\mu) = \exp \left\{ i 2\pi \operatorname{sgn}(\mu) \left| \frac{\mu}{\Omega} \right|^m \right\} \exp \left\{ -c \left| \frac{\mu}{\Omega} \right|^n \right\} \operatorname{rect} \left(\frac{\mu}{2\Omega} \right) \quad (8.28)$$

In Eq. (8.28) the letters m and n denote real positive numbers. Since the values of m are no longer integer numbers, then the first term in Eq. (8.28) represents a fractional

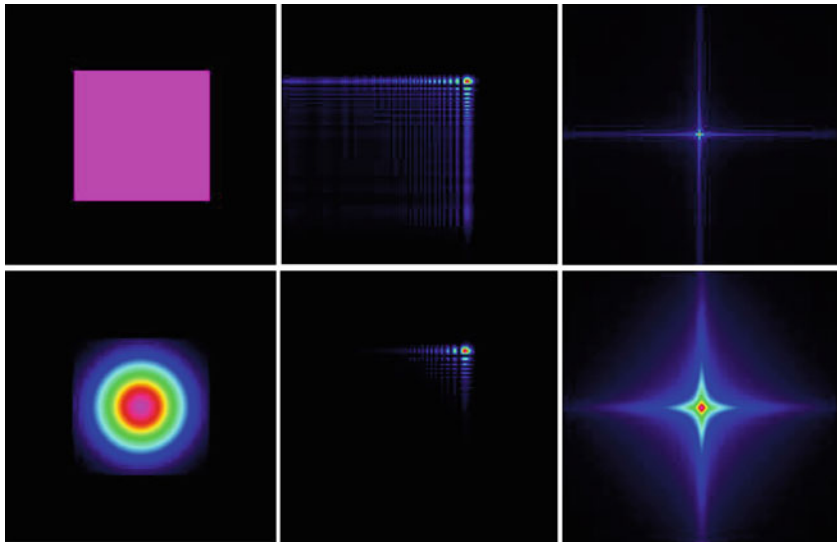


Fig. 8.13 Influence of Gaussian tapering on the pupil aperture, the PSF and the MTF

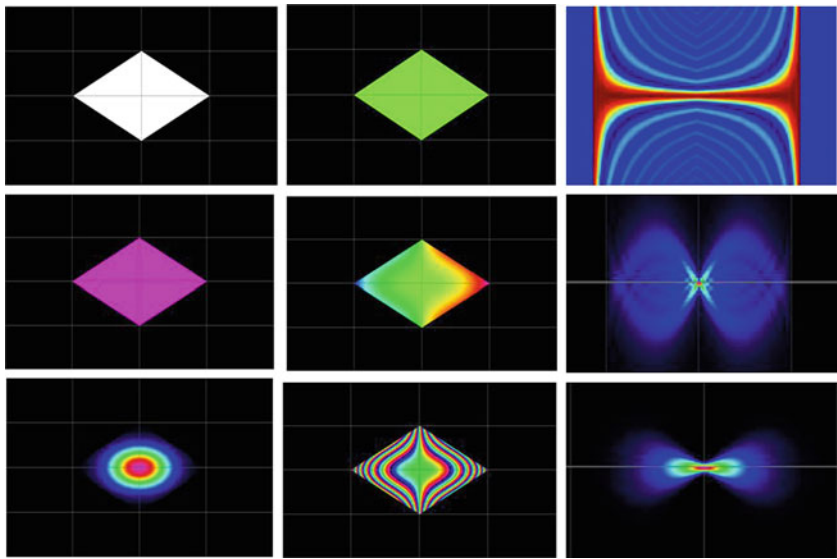


Fig. 8.14 The impact of a Gaussian apodizer on product spectrum, and the resultant ambiguity function

order wavefront. Due to the factor $\text{sgn}(\mu)$, denoting the signum function, the wavefront has phase delays that are odd functions. Furthermore, regarding the second term in Eq. (8.28), for values of n such that $n < 2$ the amplitude transmittance is denoted as sub Gaussian function; for $n = 2$, the amplitude transmittance is represented by a

Gaussian function; while for $n > 2$, the amplitude transmittance is denoted as super Gaussian function. We employ the generic word hyper Gaussian for encompassing the cases under exploration with $0 < n < 10$.

For our numerical simulations we use the following definitions that apply for the 1-D case. For variable values of focus error, the normalized irradiance distribution of the impulse response is

$$|q(x; W)|^2 = \left| \int_{-\infty}^{\infty} Q(\mu) \exp \left[i 2\pi \left(W \left(\frac{\mu}{\Omega} \right)^2 + x\mu \right) \right] \text{rect} \left(\frac{\mu}{2\Omega} \right) d\mu \right|^2. \quad (8.29)$$

And of course, the MTF is

$$|H(\mu; W)| = \int_{-\infty}^{\infty} |q(x; W)|^2 \exp(-i 2\pi \mu x) dx. \quad (8.30)$$

We evaluate numerically Eqs. (8.29) and (8.30) using the fast Fourier transform (FFT) algorithm described in reference [40]. We use 1024 points and a set of Graphic User Interface (GUI) elements. The numerical process is written in C++ language. Our numerical search starts by considering the values that were identified in the previous section. Then, we modify the parameters “a” and “c” in Eq. (8.28) until the variations of the MTF have a mean square error that is less than 10^{-4} .

Once that the 1-D sub Gaussian masks were identified, $Q(\mu)$ in Eq. (8.28), the complex amplitude transmittance of the 2-D masks are obtained as the product $Q(\mu)Q(v)$. After extensive numerical evaluations, we identify the following interesting result.

Inside the range $0 \leq W \leq 3$, one can obtain a MTF that varies slowly with focus error, by using a fractional wavefront $m = 2.75$ that has a maximum optical path difference value $a = 27$, together with a sub Gaussian mask $n = 1.75$ and attenuation factor $c = 1.61$.

In Fig. 8.15, along the second column, we plot the 1-D profiles. And along the third column, we show the following 2-D displays. In the first line, we place a pseudo color picture of the 2-D amplitude transmittance variations. In the second line, we place an interferogram of the 2-D phase variations. In the third line and the fourth line, we use pseudo color pictures for displaying the 2-D variations of the PSF and the MTF, respectively.

Finally, we note that these optical characteristics preserve the resolution associated with a full aperture. However, these results come at the expense of reducing the light gathering power by a factor slightly greater than two.

8.4 Tunable Devices for Extending the Depth of Field

According to Plummer, Baker and van Tassel [41], Kitajima was the first person that proposed to implement suggested variable optical power lenses, by using a pair of cubic phase masks [42]. Years later, Lohmann [43–45] and Alvarez [46, 47] re-discovered independently and simultaneously Kitajima’s technique .

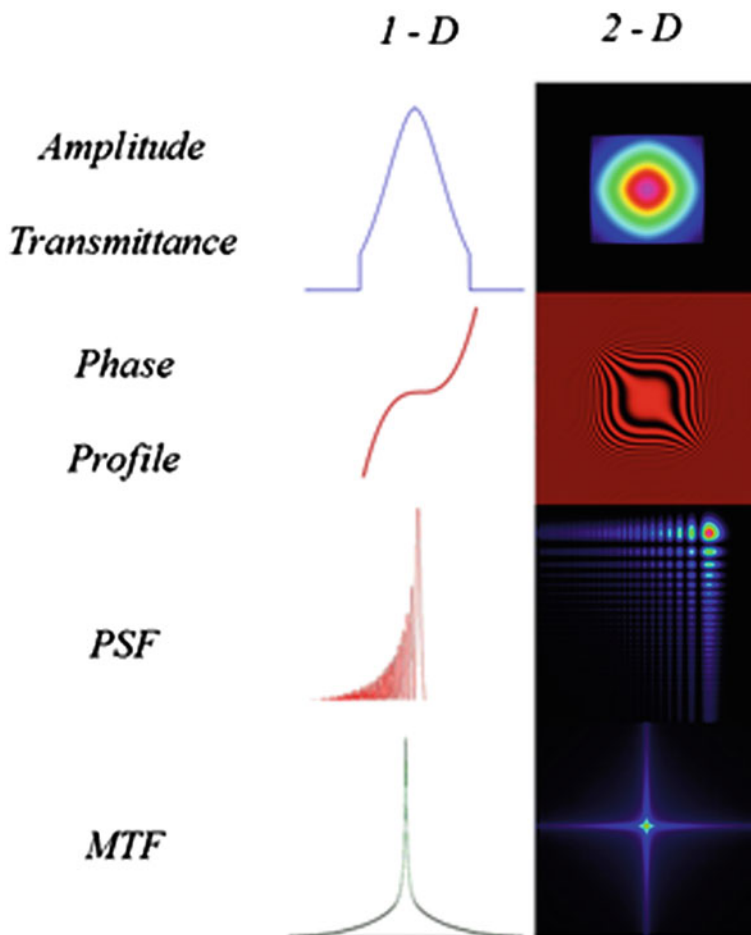


Fig. 8.15 Resultant PSF and resultant MTF associated to the hyper Gaussian apodizer in Eq. (8.28)

In what follows, our aim is threefold. First, we indicate that Kitajima's technique, commonly known as Alvarez-Lohmann lenses, is also useful for implementing tunable absorption masks, which are useful for setting hyper Gaussian apodizers with tunable half-width. Second, we show that by using two suitable helical refractive elements, one can control the optical path difference of radial focalizers. And third, we discuss the use of a pair of helical distributed amplitude masks for tuning the damping coefficient of Gaussian-like windows.

For achieving our first goal, we note that Alvarez and Lohmann lenses employ two phase masks that form a pair. The amplitude transmittance of a single mask is the complex conjugate of the other mask. Then, by introducing a lateral displacement between the two masks, say by the spatial frequency σ , one sets a varifocal lens. In mathematical terms, for the 1-D case, a single element of the pair has the following complex amplitude transmittance

$$Q(v) = \exp \left\{ i2\pi a \left(\frac{v}{\Omega} \right)^3 \right\}. \quad (8.31)$$

In Eq. (8.31) the lower case letter “a” denotes the optical path difference in units of the wavelength λ . Next, it is convenient to use two elements. Each element has the complex amplitude transmittance in Eq. (8.31). However when setting the pair, one element is the complex conjugate of the other. Then, one introduces a lateral displacement between the elements of the pair. In this manner, the overall complex amplitude transmittance is

$$\begin{aligned} P_Q(v; \sigma) &= Q \left(v + \frac{\sigma}{2} \right) Q^* \left(v - \frac{\sigma}{2} \right) \\ &= \exp \left\{ i \left(\frac{a\pi}{2} \right) \left(\frac{\sigma}{\Omega} \right)^3 + i2\pi \left(\frac{a\sigma}{\Omega} \right) \left(\frac{v}{\Omega} \right)^2 \right\}. \end{aligned} \quad (8.32)$$

In Eq. (8.32) the quadratic variation, in the variable v , is similar to the amplitude transmittance of a lens. However, it is important to recognize that by changing σ , one can tune the power of a lens.

Moreover, we recognize that the physical procedure for obtaining the result in Eq. (8.32) is similar to the mathematical operation that is involved when evaluating the OTF in Eq. (8.18). Hence, we claim the following.

By visualizing the amplitude PSF of the pair in Eq. (8.32), one visualizes the ambiguity function of a single element of the pair, as in Eq. (8.18). That is,

$$p_Q(x; \sigma) = N_{orma} \int_{-\infty}^{\infty} P_Q(v, \sigma) \exp[i2\pi x v] dv = A_Q(\sigma, x). \quad (8.33)$$

Now, we have a physical method (the use of a pair of phase masks) for understanding the influence that a single element has on the behavior of the ambiguity function.

Furthermore, one can propose the use of a mask that has phase variations to the four-power for implementing a cubic phase mask, with controllable optical path difference.

For this application, we consider that the complex amplitude transmittance of a single element is

$$Q(v) = \exp \left\{ i2\pi a \left[\left(\frac{v}{\Omega} \right)^4 - \frac{1}{2} \left(\frac{v}{\Omega} \right)^2 \right] \right\}. \quad (8.34)$$

As before, we employ a phase conjugated pair and we introduce a lateral displacement between the members of the pair. Then, we generate the following generalized pupil function

$$\begin{aligned} P_Q(v; \sigma) &= Q \left(v + \frac{\sigma}{2} \right) Q^* \left(v - \frac{\sigma}{2} \right) \\ &= \exp \left\{ i2\pi \left(\frac{4a\sigma}{\Omega} \right) \left(\frac{v}{\Omega} \right)^3 \right\} \\ &\quad \exp \left\{ i2\pi \left(\frac{a\sigma}{\Omega} \right) \left[\left(\frac{\sigma}{\Omega} \right)^2 - 1 \right] \left(\frac{v}{\Omega} \right) \right\}. \end{aligned} \quad (8.35)$$

From Eq. (8.35) one notes that by changing the value of σ , one can change the optical path difference of a cubic phase mask. In other words, we can implement a varicubic phase masks. However, the proposed phase mask generates also a linear phase variation. The influence of this unwanted term can be reduced by properly selecting the values of the initial optical path difference and the maximum value of the lateral displacement. See for example [48–50].

For achieving our second goal, in this section, we describe the use of a pair of amplitude masks that help for setting a Gaussian spatial filter, with adjustable half-width [50]. We start our discussion, by considering the amplitude transmittance of the first amplitude element of the proposed pair

$$T_1(\mu) = \exp \left\{ -c \left[1 + \left(\frac{\mu}{\Omega} \right)^3 \right] \right\} \text{rect} \left(\frac{\mu}{4\Omega} \right). \quad (8.36)$$

As before, in Eq. (8.36) we use a lower case letter “c” for denoting a dimensionless damping factor of the Gaussian function. From Eq. (8.36), we note that the length of the mask is 4Ω . At its edges the amplitude transmittance has real positive values. Now, the amplitude transmittance of the of the second mask is

$$T_2(\mu) = \exp \left\{ -c \left[1 - \left(\frac{\mu}{\Omega} \right)^3 \right] \right\} \text{rect} \left(\frac{\mu}{4\Omega} \right). \quad (8.37)$$

Again the length of the mask is 4Ω , and at its edges the amplitude transmittance has real positive values. By introducing a lateral displacement, σ ; between the masks, the overall amplitude transmittance inside the pupil aperture is

$$T(\mu; \sigma) = T_1 \left(\mu + \frac{\sigma}{2} \right) T_2 \left(\mu - \frac{\sigma}{2} \right). \quad (8.38)$$

If one substitutes Eqs. (8.36) and (8.37) in Eq. (8.38) one obtains

$$T(\mu; \sigma) = \exp \left\{ -2c \left[1 + \left(\frac{\sigma}{2\Omega} \right)^3 \right] \right\} \exp \left\{ - \left(\frac{3c\sigma}{4\Omega} \right) \left(\frac{\mu}{\Omega} \right)^2 \right\} \text{rect} \left(\frac{\mu}{2\Omega} \right). \quad (8.39)$$

It is apparent from Eq. (8.39) that inside the pupil aperture, the overall amplitude transmittance varies as a Gaussian function. Its half-width can be modified by changing the lateral amount of displacement in the Fourier domain. In reference [51] we have extended the above result to 2-D.

Here it is relevant to note that if one uses simultaneously the tunable cubic phase mask and the tunable Gaussian amplitude mask, then one has two extra degrees of freedom for setting the pre-processing filter; as was discussed in the previous section. However, we also note that so far our tunable devices are only useful when the complex amplitude profiles can be expressed as monomials to an integer power. We discuss next an optical technique for overcoming this limitation.

After proposing his varifocal technique, Lohmann applied his result for generating tunable zone plates. Lohmann and Paris have proposed the use of helical modulations [52] for generating other types of varifocal zone plates. In their proposal, Lohmann and Paris suggested the use of an average angular operation for achieving tunable devices that have only radial variations.

Later on, Burch and Williams [53] used Lohmann's technique for implementing an alignment device, which has the interesting twist of incorporating an additional phase factor as proposed for Alvarez in his varifocal technique.

Bernet and coworkers have revisited the use of *diffractive elements* for implementing varifocal lenses using helical variations [54–56]. And rather recently, some of us, have suggested the use of two helical *refractive elements* for setting several varifocal devices [57, 58]. In what follows we revisited these latter proposals.

For achieving our final goal, in this section, we note that Bryngdahl analysed interferograms in terms of polar coordinates [59]. In Fig. 8.16 we show some schematic diagrams for describing the generation of interference patterns. The interferograms are generated by superimposing a plane reference wavefront with one of the following object beams. At the top of Fig. 8.16 the object beam has quadratic radial variations; while at the middle of Fig. 8.16 the object beam has linear helical variations (angular variations). At the bottom of Fig. 8.16 the object beam has both radial as well as helical variations.

For describing the optical devices of our interest, we consider the following complex amplitude transmittance

$$Q(\rho, \varphi) = \exp\{iaR(\rho)\varphi\}. \quad (8.40)$$

In Eq. (8.40) we use the Greek letters ρ and φ for denoting the radial spatial frequency and the polar angle at the pupil aperture, respectively. The Latin letter a represents the optical path difference of the optical device. For making comparisons it is useful to remember that a lens, with fixed optical power, has the following complex amplitude transmittance

$$Q(\rho, \varphi) = \exp\left\{ia\left(\frac{\rho}{\Omega}\right)^2\right\}. \quad (8.41)$$

In Eq. (8.41) the Greek letter Ω denotes the maximum value of the radial spatial frequency. This value is typically called the cut-off spatial frequency of the pupil aperture. The interferogram of the quadratic phase variation in Eq. (8.41) is a Fresnel zone plate; as is shown in the left-hand side of Fig. 8.17.

If the lens has also helical variations then the complex amplitude transmittance is

$$Q(\rho, \varphi) = \exp\left\{ia\left(\frac{\rho}{\Omega}\right)^2\varphi\right\}. \quad (8.42)$$

At the right hand side of Fig. 8.17, we show the interference pattern that is generated between a plane wavefront and the complex amplitude transmittance in Eq. (8.42). At the left-hand side of Fig. 8.18, we show the phase variations in Eq. (8.42).

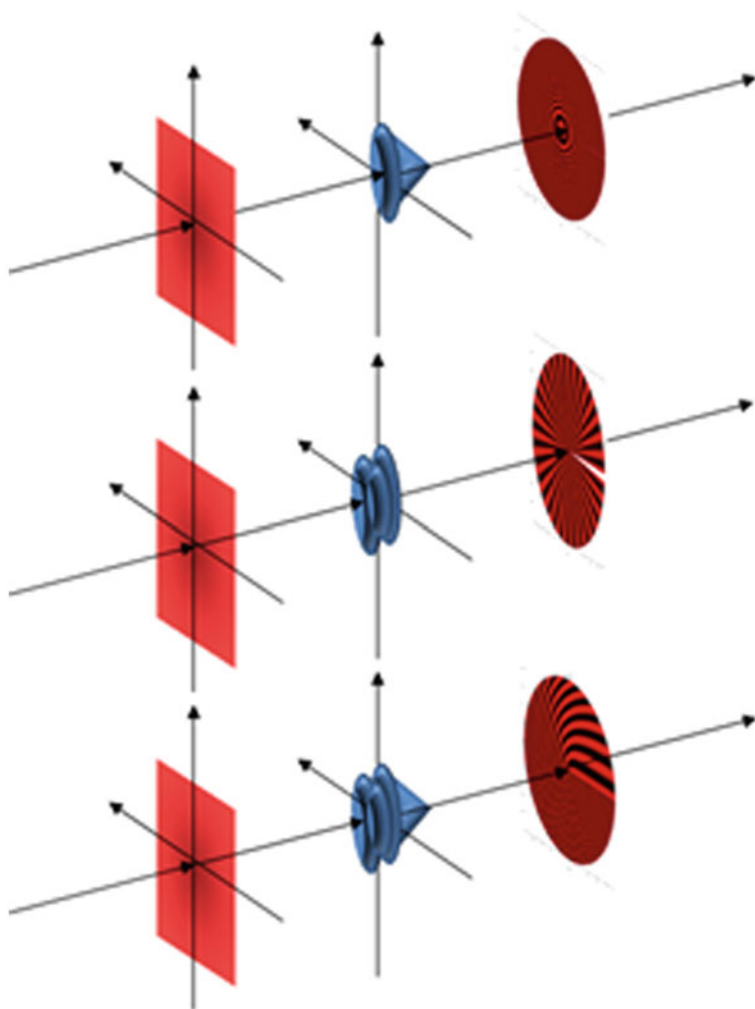


Fig. 8.16 Interferograms obtained as the interference between a reference plane wavefront and three different object beams: **a** radial beam, **b** helical beam, and **c** a beam having both radial and helical variations. The object beam is obtained after passing through the optical device

The interferogram, at the right-hand side of the same figure, was first discussed by Lohmann and Paris.

Next, we note that rather than introducing a lateral displacement between the elements of the pair (as depicted in at the left-hand side of Fig. 8.19) we can introduce an in-plane rotation between the elements of the pair (as depicted at the right-hand side of Fig. 8.19).

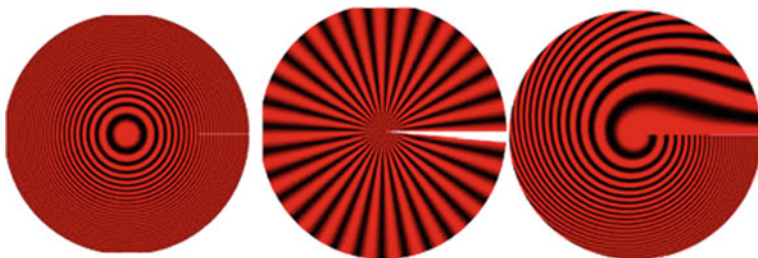


Fig. 8.17 Interference patterns that are obtained using a reference plane wavefront and three different object beams: radial beam, helical beam, and a beam having both radial and helical variations, respectively

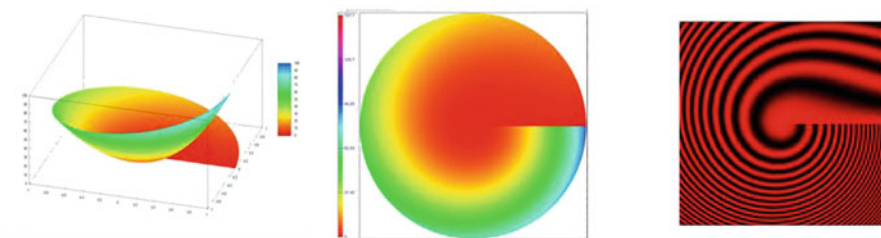


Fig. 8.18 Three different views of the helical phase in Eq. (8.41): 3-D curve, 2-D pseudo color variations and the interference pattern that is generated when using as reference beam a uniform plane wave

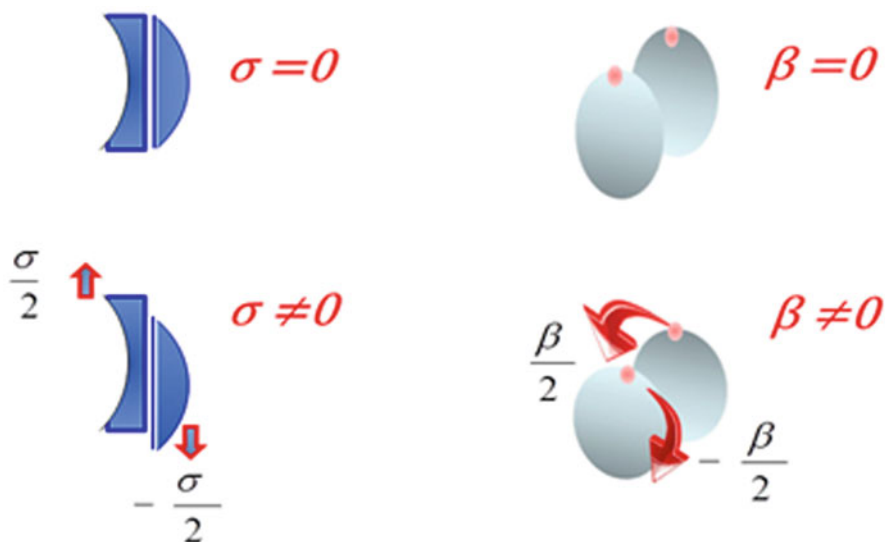


Fig. 8.19 Tunable devices using a controllable lateral shear, with spatial frequency σ , or a controllable in-plane rotation angle β

For this later application, we consider that the complex amplitude transmittance of the first refractive element is

$$T_1(\rho, \varphi) = \exp \left\{ i2\pi a\varphi \left(\frac{\rho}{\Omega} \right)^m \right\}. \quad (8.43)$$

In Eq. (8.42) the Latin letter m denotes the power of the radial variable. The complex amplitude transmittance of the second refractive element is the complex conjugate of the first element. That is,

$$T_2(\rho, \varphi) = \exp \left\{ -i2\pi a\varphi \left(\frac{\rho}{\Omega} \right)^m \right\}. \quad (8.44)$$

Now, if both refractive elements are used as a pair, and we introduce an in-plane rotation between the elements of the pair (say by an angle β) the overall complex amplitude transmittance is

$$\begin{aligned} T(\rho; \beta) &= T_1 \left(\rho, \varphi + \frac{\beta}{2} \right) T_2 \left(\rho, \varphi - \frac{\beta}{2} \right) \\ &= \exp \left\{ i2\pi a\beta \left(\frac{\rho}{\Omega} \right)^m \right\}. \end{aligned} \quad (8.45)$$

It is apparent from Eq. (8.44) that the complex amplitude transmittance of the pair is independent of the helical variable φ . Furthermore, we recognize that the angle β modifies linearly the value of the optical path difference. And in this manner, one can exploit the angular variation for controlling the optical path difference of the radial focalizer.

In Fig. 8.20, we show the use of the tunable focalizer as spatial filters in an afocal, optical processor. It is convenient to note that the proposed optical technique, as expressed in Eq. (8.44), can be extended to wide range of radial variations. In mathematical terms,

$$\begin{aligned} T(\rho; \beta) &= \exp \left\{ i2\pi a \left(\varphi + \frac{\beta}{2} \right) R(\rho) \right\} \\ &\quad \exp \left\{ -i2\pi a \left(\varphi - \frac{\beta}{2} \right) R(\rho) \right\} \\ &= \exp \{ i2\pi a\beta R(\rho) \}. \end{aligned} \quad (8.46)$$

Next we describe a method for optically tuning the half-width of hyper Gaussian apodizers; as is discussed in references [60, 61]. As depicted in Fig. 8.20, we consider that at the Fraunhofer plane we place two amplitude masks forming a pair. The amplitude transmittance of the first mask is

$$T_1(\rho, \varphi; n) = \exp \left\{ -\frac{1}{2} \left(\frac{\rho}{\Omega} \right)^n \left(1 + \frac{\varphi}{2\pi} \right) \right\} \text{circ} \left(\frac{\rho}{\Omega} \right). \quad (8.47)$$

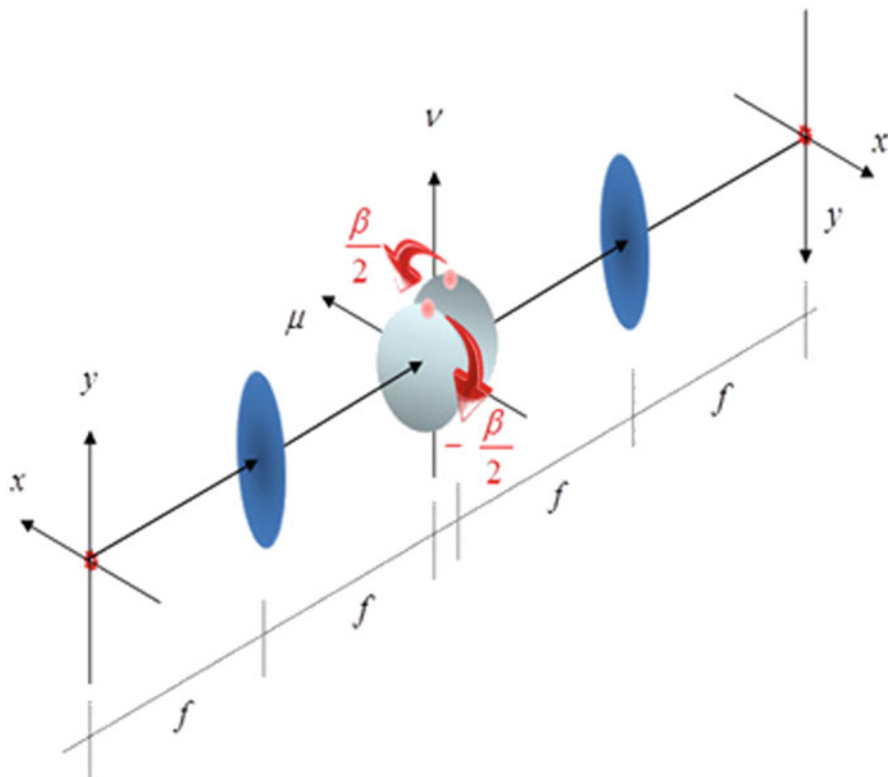


Fig. 8.20 Optical processor that employs a pair of helical masks at the Fraunhofer plane

In Eq. (8.47) the Greek letters ρ and φ denote again the polar coordinates in the pupil aperture. The maximum value of the polar coordinate, ρ , is the cut-off spatial frequency Ω . The circ function represents the pupil aperture, $0 \leq \rho \leq \Omega$. The Latin letter “n” denotes the power of the radial variable. The polar angle varies inside the interval $0 \leq \varphi < 2\pi$. We note that if $n = 2$, one has an amplitude transmittance that is proportional to a Gaussian function. A sub Gaussian mask is defined by a value of $n < 2$. And again if $n > 2$, one has super Gaussian masks. We denote as hyper Gaussian any amplitude transmittance within the range $0 < n < 10$. We recognize that the amplitude transmittance in Eq. (8.47) is bounded.

The amplitude transmittance of the second mask is

$$T_2(\rho, \varphi; n) = \exp \left\{ -\frac{1}{2} \left(\frac{\rho}{\Omega} \right)^n \left(1 - \frac{\varphi}{2\pi} \right) \right\} \text{circ} \left(\frac{\rho}{\Omega} \right). \quad (8.48)$$

Again we note that the amplitude transmittance in Eq. (8.48) is bounded. Next, we place in contact these two previously described masks for setting a pair. The overall complex amplitude transmittance becomes

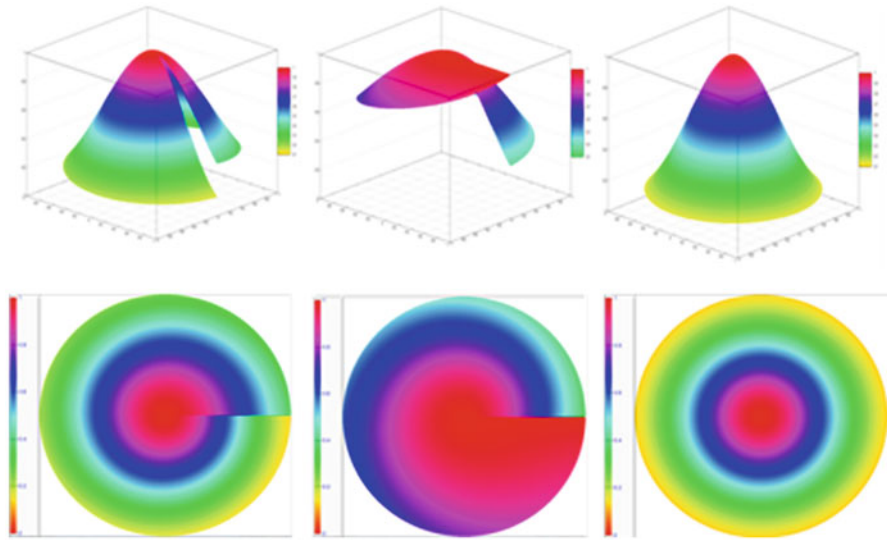


Fig. 8.21 Tuning the half-width of a Gaussian apodizer by the use of a pair of asymmetric masks that have helical amplitude variations

$$\begin{aligned}
 T(\rho; \beta) &= T_1 \left(\rho, \varphi + \frac{\beta}{2} \right) T_2 \left(\rho, \varphi - \frac{\beta}{2} \right) \\
 &= \exp \left\{ -\frac{\beta}{4\pi} R(\rho) \right\} \text{circ} \left(\frac{\rho}{\Omega} \right).
 \end{aligned} \tag{8.49}$$

From Eq. (8.49) it is clear that the overall amplitude transmittance does not longer depend on the angular variable φ . That is, the overall amplitude transmittance has radial symmetry. Furthermore, the half-width of the radially symmetric, hyper Gaussian masks can be controlled by changing the rotation angle β . This general result is illustrated for the particular case of $n = 2$, in Fig. 8.21.

Along the first line, of Fig. 8.21, we show the 3-D amplitude distributions of the transmittances in Eqs. (8.47), (8.48) and (8.49) respectively. Along the second line, of Fig. 8.21, we show the amplitude variations as 2-D color encoded pictures. It is interesting to note that the product of the asymmetrical masks in the first and second columns, of Fig. 8.21, generates the symmetrical masks shown at the third column of Fig. 8.21.

Finally, we emphasize on the many possibilities of this procedure by using the illustrations in Fig. 8.22. Along the first line we display the 1-D amplitude profiles of a sub Gaussian mask, $n = 1.5$, a Gaussian mask, $n = 2$, and super Gaussian mask, $n = 8$. The amplitude variations of these amplitude masks are shown as 2-D pictures along the second line of Fig. 8.22. Along the third line, of the same figure, we display 3-D curves.

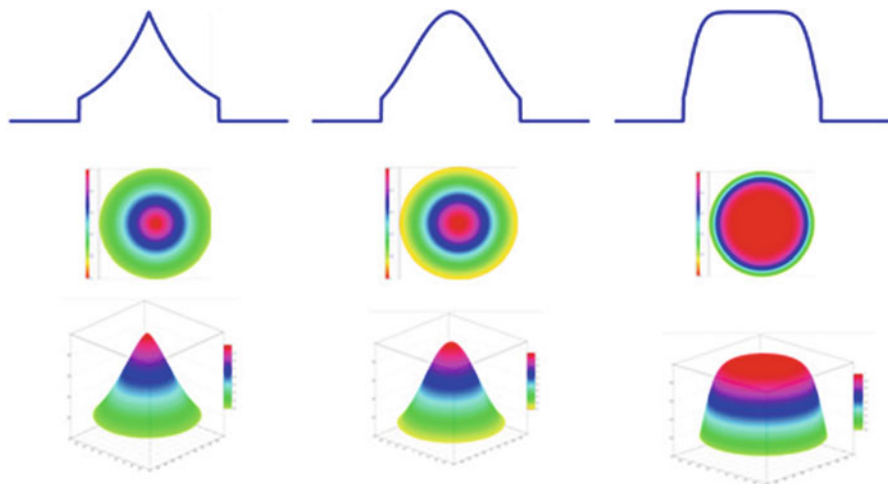


Fig. 8.22 Radially symmetric hyper Gaussian apodizer with tunable half-widths, which were generated by using a pair of masks that have helical amplitude variations

It is apparent from Eq. (8.49) and from Figs. 8.21 and 8.22 that by using a proper pair of masks, which have helical amplitude variations, one can control the half-width of a rather large set of hyper Gaussian masks. Of course, in principle one can extend the previous results to other types of apodizers.

8.5 Final Remarks

We have indicated that one can employ a rather simply optical processor for visualizing, as a 2-D picture, the evolution of a 2-D scalar wave; as is predicted by Helmholtz equation. For this type of application, one needs to use a very narrow slit that follows a semicircle over an otherwise opaque mask.

Then, we have noted that within the paraxial regime, Helmholtz equation has a different expression. Hence, for visualizing the evolution of the point spread function with focus error, one needs to use a very narrow slit that follows now a parabolic curve.

The above results were extended for visualizing the influence that the optical path difference (of certain phase mask) has over the point spread function of an optical system. We have discussed the use of another optical processor for obtaining displays that describe the impact of the optical path difference over the modulation transfer function.

Then, we have discussed the use of anamorphic processors for visualizing the generation of the ambiguity function of a 1-D pupil mask. We have related this method with the visualization of the optical transfer function with variable focus

errors. When analyzing nonconventional devices using the ambiguity function, it is convenient to take into account the results obtained using the narrow slits.

Next, we have noted that the mathematical tools employed for describing the ambiguity function have a physical counterpart when using two refractive elements forming a pair, for implementing varifocal lenses; here denoted as Alvarez-Lohmann lenses. We have shown that the Alvarez-Lohmann lenses have an equivalent, when setting Gaussian apodizers with variable half-width.

We have indicated that the use of a pair of refractive elements, for controlling the optical power of a lens, leads to optical elements with helical phase variations. We have shown that one can control the optical path difference of a wide range of radial focalizers, if one uses a pair of refractive elements that have both helical phase variations and radial phase variations. To this end, one introduces an in-plane rotation between the refractive elements of the pair.

Finally, based on the previous results, we have discussed the use of two masks that have helical and radial amplitude variations for setting a large set of hyper Gaussian apodizers, with tunable half-width. Again for this application, one needs to introduce an in-plane rotation between the amplitude elements of the pair.

Acknowledgements We gratefully acknowledge the financial support of CONACYT, grant 157673, Fondo: I0017, as well as the grant 1477-CIO-UG-2013, DAIP, University of Guanajuato.

References

1. Jacquinot, P.: Apodization, Appendix E, in concepts of classical optics, John Strong, pp. 410–418. W. H. Freeman, San Francisco (1958)
2. Marechal, A., Françon, M.: Diffraction Structure Des Images, pp. 152–155. Masson, Paris (1970)
3. Papoulis, A.: Systems and Transforms with Applications in Optics, pp. 442–444. McGraw-Hill, New York (1968)
4. Steel, W.H.: Interferometry, pp. 23, 234, 248–249. Cambridge University Press, Cambridge (1983)
5. Goodman, J.W.: Introduction to Fourier Optics, pp. 151–154. McGraw-Hill, New York (1996)
6. Ojeda-Castañeda, J., Berriel-Valdos, L.R., Montes E.: Bessel annular apodizers: imaging characteristics. *Appl. Opt.* **26**(10), 2770–2772 (1987)
7. McCutchen, C.W.: Generalized aperture and three-dimensional diffraction image. *J. Opt. Soc. Am.* **54**(2), 240–244 (1964)
8. Ojeda-Castañeda, J., Berriel-Valdos, L.R.: Arbitrarily high focal depth with finite apertures. *Opt. Lett.* **13**(3), 183–185 (1988)
9. Ojeda-Castañeda, J., Andres, P., Diaz, A.: Strehl ratio with low sensitivity to spherical aberration. *J. Opt. Soc. Am. A* **5**(8), 1233–1236 (1988)
10. Ojeda-Castañeda, J., Tepichin, E., Pons, A.: Apodization of annular apertures: Strehl ratio. *Appl. Opt.* **27**(24), 5140–5145 (1988)
11. Mino, M., Okano, Y.: Improvement in the OTF of a defocused optical system through the use of shaded apertures. *Appl. Opt.* **10**(10), 2219 (1971)
12. Hauesler, G.: A method to increase the depth of focus by two step image processing. *Opt. Commun.* **6**(1), 38–42 (1972)
13. Chung, C.S., Hopkins, H.H.: Influence of nonuniform amplitude on the optical transfer function. *Appl. Opt.* **28**(6), 90–91 (1989)

14. Ojeda-Castañeda, J., Yépez-Vidal, E., Gómez-Sarabia, C.M.: Multiple-frame photography for extended depth of field. *Appl. Opt.* **52**(10), D84–D90 (2013)
15. Lohmann, A.W., Ojeda-Castañeda, J., Serrano-Heredia, A.: Trading dimensionality in signal processing. *Opt. Laser Technol.* **28**(2), 101–107 (1996)
16. Ojeda-Castañeda, J., Lohmann, A.W.: Young's experiment in signal synthesis, Chapter 14, *Trends in Optic*, Anna Consortini Editor, pp. 263–280. Academic Press, San Diego (1996)
17. Lohmann, A.W., Ojeda-Castañeda, J., Frausto, C.: Optical simulation of free-space propagation. *Opt. Commun.* **157**(1–6), 7–12 (1998)
18. Ojeda-Castañeda, J., Castro, A.: Simultaneous Cartesian coordinate display of defocused optical transfer functions. *Opt. Lett.* **23**(13), 1049–1051 (1998)
19. Woodward, P.M.: Radar ambiguity analysis, Technical Note No. 731. Royal Radar Establishment, London (1967)
20. Papoulis, A.: Ambiguity function in Fourier optics. *J. Opt. Soc. Am.* **64**(6), 779–788 (1974)
21. Guigay, J.P.: The ambiguity function in diffraction and isoplanatic imaging by partially coherent beams. *Opt. Commun.* **26**(2), 136–138 (1978)
22. Marks, R.J., Walkup, J.K., Krile, T.F.: Ambiguity function display: an improved coherent processor. *Appl. Opt.* **16**(3), 746–750 (1977)
23. Brenner, K.-H., Lohmann, A.W., Ojeda-Castañeda, J.: The ambiguity function as a polar display of the OTF. *Opt. Commun.* **44**(5), 323–326 (1983)
24. Ojeda-Castañeda, J., Berriel-Valdos, L.R., Montes, E.: Ambiguity function as a design tool for high focal depth. *Appl. Opt.* **27**(4), 790–795 (1988)
25. Ojeda-Castañeda, J., Noyola-Isgleas, A.: High focal depth by apodization and digital restoration. *Appl. Opt.* **27**(12), 2583–2586 (1988)
26. Dowski, E.R., Cathey, T.W.: Extended depth of field through wave-front coding. *Appl. Opt.* **34**(11), 1859–1865 (1995)
27. Cook, C. E., Bernfeld, M.: *Radar Signals: An Introduction to Theory and Applications*, pp. 59–108. Arctech House, Norwood (1993)
28. George, N., Chi, W.: Extended depth of field using a Logarithmic asphere. *J. Opt. Pure Appl.* **5**, s157–s163 (2003)
29. Muyo, G., Harvey, A.R.: Decomposition of the optical transfer function: wavefront coding imaging systems. *Opt. Lett.* **30**(20), 2715–2717 (2005)
30. Saucedo-Carvajal, A., Ojeda-Castañeda, J.: High focal depth with fractional-power wave fronts. *Opt. Lett.* **29**(6), 560–562 (2004)
31. Castro, A., Ojeda-Castañeda, J.: Asymmetric phase masks for extended depth of field. *Appl. Opt.* **43**(17), 3474–3479 (2004)
32. Ojeda-Castañeda, J.: Focus error operator and related special functions. *J. Opt. Soc. Am.* **73**(8), 1042–1047 (1983)
33. Ojeda-Castañeda, J., Boivin, A.: The influence of wave aberrations: an operator approach. *Can. J. Phys.* **63**(2), 250–253 (1985)
34. Ojeda-Castañeda, J., Noyola-Isgleas, A.: Differential operator for scalar wave propagation. *J. Opt. Soc. Am. A* **5**(10), 1605–1609 (1988)
35. Ojeda-Castañeda, J., Berriel-Valdos, L.R., Montes, E.: Ambiguity function as a design tool for high focal depth. *Appl. Opt.* **27**(4), 790–795 (1988)
36. Marks, R.J. II, Walkup, J.K., Krile, T.F.: Ambiguity function display: an improved coherent processor. *Appl. Opt.* **16**(3), 746–750 (1977)
37. Castro, A., Ojeda-Castañeda, J., Lohmann, A.W.: Bow-tie effect: differential operator. *Appl. Opt.* **45**(30), 7878–7884 (2006)
38. Ojeda-Castañeda, J., Yépez-Vidal, E., García-Almanza, E.: Complex amplitude filters for extended depth of field. *Photonics Lett. Pol.* **2**, 162–164 (2010)
39. Ojeda-Castañeda J., Ledesma S. and Gomez-Sarabia C. M., Hyper Gaussian Windows with fractional wavefronts. *Photonics Lett. Pol.* **5**(1), 23–25 (2013)
40. Brenner, N., Rader, C.: *IEEE Acoustics. Speech Signal Process.* **24**, 264–266 (1976)
41. Plummer, W.T., Baker, J.G., van Tassel, J.: Photographic optical systems with nonrotational aspheric surfaces. *Appl. Opt.* **38**(16), 3572–2592 (1999)

42. Kitajima, I.: "Improvement in lenses". British Patent 250, 268 (July 29, 1926)
43. Lohmann, A.W.: Lente a focale variabili. Italian Patent 727, 848 (June 19, 1964)
44. Lohmann, A.W.: Improvements relating to lenses and to variable optical lens systems formed for such a lens. Patent Specification 998,191, London (1965)
45. Lohmann, A.W.: A new class of varifocal lenses. *Appl. Opt.* **9**(7), 1669–1671 (1970)
46. Alvarez, L.W.: Two-element variable-power spherical lens. US Patent 3, 305, 294 (December 3, 1964)
47. Alvarez, L.W., Humphrey, W.H.: Variable power lens and system. US Patent 3, 507, 565 (April 21, 1970)
48. Ojeda-Castañeda, J., Landgrave, J.E.A., Gómez-Sarabia, C.M.: The use of conjugate phase plates in the analysis of the frequency response of optical systems designed for an extended depth of field. *Appl. Opt.* **47**(22), E99–E105 (2008)
49. Ojeda-Castañeda, J., Aguilera Gómez, E., Plascencia Mora, H., Torres Cisneros, M., Ledesma Orozco, E.R., León Martínez, A., Pacheco Santamaría, J.S., Martínez Castro, J.G.: Carlos Salas Segoviano R., U. S. Patent 8, 159, 573B2 (April 17, 2012)
50. Ojeda-Castañeda, J., Gómez-Sarabia, C.M.: Key concepts for extending the depth of field with high resolution. *Opt. Pura Apl.* **45**(4) 449–459 (2012)
51. Ojeda-Castañeda, J., Yépez-Vidal, E., García-Almanza, E., Gómez-Sarabia, C.M.: "Tunable Gaussian mask for extending the depth of field". *Photonics Lett. Pol.* **4**(3), 115–117 (2012)
52. Lohmann, A.W., Paris, D.P.: "Variable Fresnel Zone Pattern" *Appl. Opt.* **6**(9), 1567–1570 (1967)
53. Burch, J.M., Williams, D.C.: Varifocal moiré zone plates for straightness measurement. *Appl. Opt.* **16**(9), 2445–2450 (1977)
54. Bernet, S., Jesacher, A., Fuerhapter, S., Maurer, C., Ritsch-Marte, M.: "Quantitative imaging of complex samples by spiral phase contrast microscopy". *Opt. Express* **14**(9) 3792–3805 (2006)
55. Jesacher, A., Fürhapter, S., Bernet, S., Ritsch-Marte, M.: "Spiral interferogram analysis". *J. Opt. Soc. Am. A* **23**(6) 1400–1409 (2006)
56. Bernet, S., Ritsch-Marte, M.: "Optical device with a pair of diffractive optical elements". US Patent 0134869 A1 (June 3, 2010)
57. Ojeda-Castañeda, J., Ledesma, S., Gomez-Sarabia, C.M.: Tunable apodizers and tunable focalizers using helical pairs. *Photonics Lett. Pol.* **5**(1), 20–22 (2013)
58. Ojeda-Castañeda, J., Gomez-Sarabia, C.M., Ledesma, S.: Tunable focalizers: axicons, lenses and axilenses, Tribute to H. John Caulfield, SPIE Proceedings 8833, 88330601–88330606 (2013)
59. Bryngdahl, O.: Radial- and circular-fringe interferograms. *J. Opt. Soc. Am.* **63**(9), 1098–1104 (1973)
60. Ojeda-Castañeda, J., Ledesma, S., Gomez-Sarabia, C.M.: Hyper Gaussian Windows with fractional wavefronts. *Photonics Lett. Pol.* **5**(1), 23–25 (2013)
61. Ojeda-Castañeda, J., Ledesma, S., Gomez-Sarabia, C.M.: Helical apodizers for tunable hyper Gaussian masks, Novel Optical System Design and Optimization XVI, SPIE Proceedings 8842, 88420N-1-88420N-6 (2013)

Index

A

Adaptive optics, 174
 Alcohol solutions, 203, 204, 208
 All-optical flip-flop operation, 3, 4, 15
 All-Optical Header Recognition and Packet Switching, 13–15
 All-optical memory operation of 980-nm, 10
 All-optical retiming, 1, 5, 6
 All-optical signal processing, 5
 application, 2
 All-optical signal regeneration, 5, 6
 All-optical signal-processing systems, 1
 All-optical switch, 13, 14
 Ambiguity function, 118, 125, 127–130, 143
 Analytical solution, 22, 36, 40, 42
 Anamorphic processor, 127, 128, 143
 APD, 6
 Attosecond
 pulse train, 215, 216
 pulses, 213, 216
 streak camera, 216
 streaking, 216–218, 222, 224, 228

B

Bandwidth, 6, 23, 29, 72, 78, 79, 164
 Bistable laser diodes, 1, 2, 5
 Bleaching, 207, 211
 Bolometer, 174, 177, 184–186, 188–190, 192, 194
 transformation characteristic, 184–186, 189
 Boundary conditions, 38, 40
 Bow-tie effect, 129

C

Capillary, 103–105, 107, 109, 205
 Capillary action, 103, 105, 106, 109–111

Characteristics, 71, 165, 171
 lasing, 204
 photoluminescence, 202
 polarization, 202
 polarization-bistable, 14, 16
 spatial, 80
 spectral, 208, 211
 Cladding, 20, 28, 29
 Clock pulses, 5
 Coherent processor, 119, 122, 123
 Complex amplitude distribution, 120, 122, 125, 128
 Complex amplitude transmittance, 118, 120, 126, 130, 131, 133–135, 137, 140, 141
 Confinement layer, 3
 Contact angle, 102, 104, 111
 Coulomb-laser coupling (CLC), 217, 225, 227, 228
 Coupled resonators, 42
 Cubic phase masks, 130, 133, 136

D

Data pulses, 14
 Data signal, 5, 6, 8, 9, 14
 Data signal power, 9, 10
 Data signal train, 12
 DCM, 203, 204, 207, 208, 211
 Deformable mirrors, 180, 181
 Depth of field, 117, 118, 130, 133
 Diaphragm array, 176
 Dispersion, 40, 72, 160, 161, 169, 217
 Distributed feedback (DFB)
 laser emission, 202
 Double-clad Ytterbium-doped fiber (DCYDF), 24

Drying control chemical additive (DCCA), 204, 205
 Dye molecules, 201, 202, 205
 Dyes, 204, 206–208, 211

E

Erbium-doped fiber (EDF), 27
 Erbium-doped fiber laser (EDFL), 27
 Ethanol solution, 204, 208
 Excited modes, 21, 22, 41, 43

F

Fast Fourier Transform (FFT), 133, 175
 Feedback, 25, 202
 Femtosecond laser, 102–105, 109–111
 Femtosecond laser ablation, 102
 Femtosecond laser processing, 102, 106, 110, 112
 Femtosecond laser pulses, 102, 105
 Femtosecond laser surface nano/microstructuring, 104, 111
 Ferrule, 25–27
 Fiber lasers, 19, 24, 31
 Flashlamp-pumped dye laser (FLPDL), 204
 Flatness, 167, 170
 Flip-flop devices, 2
 Flip-flop operation
 with low power consumption, 3, 5
 Fluorescence, 201, 202
 Four wave mixing (FWM), 160, 167, 169, 170
 Four-bit data signal, 11, 12
 Fractional order, 132
 Fraunhofer domain, 123
 Fraunhofer plane, 119, 120, 122, 140
 Frequency detuning, 9, 14
 Frequency shift, 35, 42
 Fresnel diffraction patterns, 129

G

Gate operation, 5, 8
 Gaussian apodizer, 130, 134, 140, 144
 Gaussian function, 132, 136, 141
 Glass dispersed liquid crystal (GDLC), 202
 Group velocity dispersion (GVD), 161, 167
 Guided modes, 22

H

Hartmann sensor, 174, 176
 based on film technology, 178
 based on IR bolometer camera, 177, 178
 Header length, 2
 Header Payload, 14
 Header recognition, 2
 Headers, 14

Helical variations, 137
 High harmonic generation (HHG), 214, 215
 High-temperature steam, 3
 Higher-order modes, 81, 82
 Hydrophilic, 102
 Hydrophilicity, 103–105, 109

I

Impulse response, 119, 123, 133
 Initial value problem, 38, 42
 Injected data signal, 9
 Injection light, 6
 Injection power, 5, 8, 9, 13
 Interferograms, 137
 Interferometer, 13, 72–74, 76, 79, 173
 Interferometer mirrors, 74
 Inversion, 41, 81
 Irradiance distributions, 120, 123

L

Laplace transform domain, 36, 40, 46
 Laser
 dyes, 203, 205, 211
 resonator, 73, 74, 76
 Lasing modes, 3
 Lasing polarization, 4, 6, 13
 LK678, 203, 204, 207

M

Magnetic field, 37, 38, 43
 Maxwell's equations, 37, 38
 Memory, 7
 four-bit optical buffer, 11–13
 operating conditions of, 9
 Microchannels, 105, 110
 Microchip laser, 71, 72, 77–79, 160, 162
 Microfluidics, 103, 105, 112
 Microgrooves, 103–106, 109, 111
 Microstructured, 170
 MMF lengths, 30
 MMI device, 20, 23, 27, 31
 spectral response of, 23
 MMI filters
 tunable, 30, 32
 Mode number, 42, 75, 76
 Modulation, 35, 45, 46, 202, 216
 Modulation Transfer Function (MTF), 125, 130, 133, 143
 Multimode fiber (MMF), 20–23, 25, 28–30
 Multimode interference (MMI)
 effects, 2, 20

N

Nano/microfluidics, 103, 110, 112
Nanostructures, 102, 105, 213
No-Core fiber, 20, 25, 26, 28, 30
Nonlinear effects, 160, 161, 168

O

Object beams, 137
Operating wavelength, 22, 24
Optical buffer memory, 2, 7
 four-bit, 11, 15
 multi-bit, 13
Optical elements, 144, 165, 173
Optical fibers, 28, 161, 164
 multimode interference in, 20
Optical gates, 8
Optical image, 105
Optical memories, 16
Optical packet, 2
Optical packet switch node, 2
Optical path difference, 118, 122, 123, 125,
 134, 136, 140, 144
Optical processor, 118–120, 122, 123, 143
Optical pulses, 12, 14
Optical signals, 2, 8
Optical spectrum analyzer (OSA), 27, 30, 166
Optical systems, 117
Optical transfer function (OTF), 118, 125, 128
Organically modified silicate gel glasses
 (ORMOSILs), 200
Output plane, 122–124, 126, 128
Output ports, 2, 13
Output power, 4, 10, 12, 25, 31, 165
Output SMF, 21, 23, 27
Oxidation, 3
Oxide, 3, 15

P

Packets, 2, 217
Passive cooling system, 180
Passive switch, 72, 77, 80, 83
Payloads, 2, 14
Performing, 6, 221
Phase masks, 123, 135
Photonic crystal fibers (PCFs), 159, 160,
 164, 165
Photonic crystals, 35
Photostability, 200, 203
Point Spread Function (PSF), 117, 130, 135
Polarization axis, 6, 14
Polarization beam combiner (PBC), 14
Polarization bistability, 1, 3
Polarization states, 1, 14

Polarization-bistable VCSELs, 1–3, 5, 7, 10,
 13–15

Polarization-switching, 8

Polarizer, 6, 8, 9, 13, 14, 165, 166

Power consumption, 4

Product Spectrum, 128–130

Protonation, 206, 207, 211

Pupil aperture, 117, 118, 122, 126, 130, 131,
 136, 137, 141

Pupil mask, 126, 127, 143

R

Reconstruction of Attosecond harmonic

 Burst By Interference in Two-photon

 Transitions (RABITT), 215, 217

Refractive index (RI), 20, 22, 25, 28, 30

Regenerated signal, 5, 6

Relative RMSD, 186–188, 190, 192

Relative root-mean-square deviations (RMSD),
 185, 186, 193, 196

Reset pulses, 5, 10, 14

Residues, 41

Resonator, 35, 36, 41, 208

Rhodamine 6G (Rh6G), 201, 203, 207, 211

S

Scalar wave, 118, 120

Self-images, 20, 21

Self-phase modulation (SPM), 161

Sensors, 20, 28, 35, 103, 160, 171, 173, 200

Set pulses, 7, 9, 10, 14

Side-mode suppression ratio (SMSR), 31

Silica gels, 205

Single mode fibers (SMF), 20, 21, 23, 25, 28

SiO₂ matrix, 208

Sol-gel, 200–202, 204

Space-to-time converter, 8, 11, 12

Spatial frequency, 118, 119, 125, 126, 134,
 137, 141

Spectral response, 20

 of MMI devices, 23

Spurious oscillations, 125, 130, 131

Standard, 21, 27, 160, 203

Stimulated Brillouin Scattering (SBS), 160, 161

Stimulated Raman Scattering, 214

Supercontinuum generation (SG), 159, 160

Supercontinuum spectrum, 164, 167, 171

Superhydrophobic, 101–103

Superposition, 40, 43, 129, 175

Superwicking surfaces, 103

 spreading of liquid on, 105, 107, 109

Switching, 13, 14

Switching power, 9, 12

Synchronization, 110

T

Tetramethoxysilane (TMOS), 203, 204, 207, 211
 Thermal lens, 72, 74, 78
 Thin film, 174, 176, 178, 203
 Thin film technology
 sensor based on, 178, 180
 Threshold, 3, 6–8, 80, 200, 207
 Time-dependent Schrödinger equation (TDSE), 217, 227
 Time-to-space converter, 7, 11
 Timing jitter, 5, 6
 TR waves, 39, 41, 45
 Transmission, 20, 23, 30
 Tunable
 MMI fiber lasers, 24
 ferrule based tunable laser, 25–27
 free space tunable laser, 24, 25
 Tunable devices
 for extending the depth of field, 133, 135–138, 140–142
 Tunable fiber laser

 liquid level, 29–31

Tuning mechanism, 24–27, 30
 Tuning range, 25–27, 30, 31

U

Ultrafast, 7, 8, 15, 108, 213, 214

V

Vertical-cavity surface-emitting lasers (VCSELs), 1, 7, 11

W

Wavefront sensors, 173, 174, 181
 Wavelength division multiplexer (WDM), 27
 Wavelength tuning, 23, 25, 28, 29, 31
 Wettability, 110, 111
 Wetting properties, 101, 102, 110
 Whispering gallery (WG), 35
 Wigner time delay, 219–221, 224

Y

YAG laser, 165, 167